

The preferentially magnified active nucleus in IRAS F10214+4724 – III. VLBI observations of the radio core

R.P. Deane^{1,2*}, S. Rawlings¹, M.A. Garrett^{3,4}, I. Heywood¹, M.J. Jarvis^{1,5,6},
H.-R. Klöckner^{1,7}, P.J. Marshall¹, J.P. McKean³

¹*Astrophysics, Department of Physics, University of Oxford, Keble Road, Oxford, OX1 3RH, UK*

²*Astrophysics, Cosmology and Gravity Centre, Department of Astronomy, University of Cape Town, Private Bag X3, Rondebosch 7701, South Africa*

³*ASTRON, The Netherlands Institute for Radio Astronomy, Postbus 2, 7990 AA, Dwingeloo, The Netherlands*

⁴*Leiden Observatory, Leiden University, Postbus 9513, 2300 RA Leiden, The Netherlands*

⁵*Centre for Astrophysics Research, Science & Technology Research Institute, University of Hertfordshire, Hatfield, AL10 9AB, UK*

⁶*Physics Department, University of the Western Cape, Cape Town, 7535, South Africa*

⁷*Max-Planck-Institut für Radioastronomie, Auf dem Hügel 69, 53121 Bonn, Germany*

Accepted 2013 July 6

ABSTRACT

We report 1.7 GHz Very Long Baseline Interferometry (VLBI) observations of IRAS F10214+4724, a lensed $z = 2.3$ obscured quasar with prodigious star formation. We detect what we argue to be the obscured active nucleus with an effective angular resolution of < 50 pc at $z = 2.3$. The $S_{1.7} = 210 \mu\text{Jy}$ ($9\text{-}\sigma$) detection of this unresolved source is located within the *HST* rest-frame ultraviolet/optical arc, however, $\gtrsim 100$ milli-arcseconds northward of the arc centre of curvature. This leads to a source plane inversion that places the European VLBI Network detection to within milli-arcseconds of the modelled cusp caustic, resulting in a very large magnification ($\mu \sim 70$), over an order of magnitude larger than the CO (1 \rightarrow 0) derived magnification of a spatially resolved *JVLA* map, using the same lens model. We estimate the quasar bolometric luminosity from a number of independent techniques and with our X-ray modelling find evidence that the AGN may be close to Compton-thick, with an intrinsic bolometric luminosity $\log_{10}(\langle L_{\text{bol,QSO}} \rangle / L_{\odot}) = 11.34 \pm 0.27$ dex. We make the first black hole mass estimate of IRAS F10214+4724 and find $\log_{10}(M_{\text{BH}}/M_{\odot}) = 8.36 \pm 0.56$ which suggests a low black hole accretion rate ($\lambda = \dot{M}/\dot{M}_{\text{Edd}} \sim 3 \pm 7$ percent). We find evidence for a $M_{\text{BH}}/M_{\text{spheroid}}$ ratio that is 1-2 orders of magnitude larger than that of submillimetre galaxies (SMGs) at $z \sim 2$. At face value, this suggests IRAS F10214+4724 has undergone a different evolutionary path compared to SMGs at the same epoch. A primary result of this work is the demonstration that emission regions of differing size and position can undergo significantly different magnification boosts (> 1 dex) and therefore distort our view of high-redshift, gravitationally lensed galaxies.

Key words: gravitational lensing: strong, galaxies: evolution, galaxies: active

1 INTRODUCTION

Two major empirical results in the last 15 years have greatly increased the need to characterise the black hole accretion history of the Universe, in particular in the redshift range $z \sim 2 - 3$ where the cosmic star formation and black hole accretion rate densities appear to peak (e.g. Madau et al. 1996; Dunlop & Peacock 1990). The first of these breakthroughs is the finding that super-massive black hole masses are strongly correlated with their host galaxy spheroid luminosity and stellar velocity dispersion (Magorrian et al. 1998; Gebhardt et al. 2000; Ferrarese & Merritt 2000). The sec-

ond is the realisation that most ($\gtrsim 70$ percent) black hole accretion is obscured (e.g. Martínez-Sansigre et al. 2005; Gilli et al. 2007). Not only is the role of super-massive black holes more fundamental than previously thought, but our view of this fundamental process is largely hidden for the majority of active galaxies. This has driven a number of (necessarily multi-wavelength) observation programmes to characterise this population of ‘obscured’ quasars, with a focus on the X-ray and mid-infrared windows (e.g. Polletta et al. 2006; Fiore et al. 2008). However, these regions of the electromagnetic spectrum have their challenges and contaminants, predominately due to Compton-thick column densities; the level of torus and/or host galaxy obscuration; and the unknown contribution of star formation to mid-infrared dust heating. In this regard, high resolution

* E-mail: roger.deane@astro.ox.ac.uk

radio imaging provides a direct method of disentangling the AGN and star formation components through the measurement of brightness temperature and the radio spectral index.

This was demonstrated by Klöckner et al. (2009) who showed a sample of eleven $z \gtrsim 2$ obscured quasars to be radio intermediate luminosity quasars ($L_{5\text{GHz}} = 10^{23-24} \text{ W Hz}^{-1} \text{ sr}^{-1}$), a challenging observation for VLBI arrays. Until the previous decade, VLBI was an observational technique used almost exclusively to detect bright ($\gtrsim 10 \text{ mJy}$) radio sources which could be self-calibrated to improve the image quality and dynamic range. However, due to a confluence of factors - technical and scientific - VLBI has entered the sub-mJy domain.

In this work, we exploit the unique advantage of VLBI observations to isolate high brightness temperature emission at milli-arcsecond scales and constrain the active core flux and position in a high-redshift, gravitationally lensed obscured quasar. While large-scale VLBI surveys will only be possible with the full *Square Kilometre Array (SKA)*, current studies of individual systems (particularly lensed systems) provide a preview of the science that will be possible with a large sample size in a decade. In addition, a larger sample of unlensed systems from the *Herschel ATLAS* catalogue (Eales et al. 2010) have been observed with the *EVN* (Virdee et al., in preparation), a study that is important since it is free from any magnification bias and preferential magnification effects.

This paper is the third in a series on the gravitationally lensed, obscured quasar IRAS F10214+4724 (IRAS 10214 hereafter). IRAS 10214 is a well-studied galaxy that is often used as an archetype high-redshift ULIRG, largely because of its extensive multi-wavelength coverage and its early discovery in 1991 (Rowan-Robinson et al. 1991). It radiates $\gtrsim 95$ percent of its bolometric luminosity in the infrared, the intrinsic source of which is poorly constrained. IRAS 10214 is classified as a cusp-caustic lens that results in a large arc to the south of the lens galaxy, and a small counter-image to the north of the lens (see Eisenhardt et al. 1996). In Deane et al. (2013, **D13a** hereafter) we derived a new lens model for IRAS 10214 based on a deep *HST* F814W map and introduced methods to investigate preferential magnification. In Deane et al. (2013b, **D13b** hereafter) we report a spatially resolved CO (1 \rightarrow 0) *JVLA* observation that, by proxy, provides an estimate of the magnification of the star formation component in IRAS 10214.

In this work we focus on the AGN properties of IRAS 10214. Previous observations have provided strong arguments that IRAS 10214 hosts an obscured quasar. The primary pieces of evidence supporting this are as follows.

(i) The observed optical continuum emission is highly polarised, implying that this is predominately scattered rest-frame ultraviolet light from a dust-embedded source (Lawrence et al. 1993).

(ii) Optical spectra show a wide range in ionisation, supporting the view that the galaxy hosts an active nucleus (Elston et al. 1994; Soifer et al. 1995)

(iii) There are clear broad emission lines present in the polarised spectrum which are typical of quasars (Goodrich et al. 1996).

Despite these strong pieces of evidence, X-ray observations did not confirm the X-ray luminosity (L_X) expected in IRAS 10214, particularly when compared with the measured [O III] $\lambda 5007$ luminosity which is correlated with L_X for type I AGN (Alexander et al. 2005; Iwasawa et al. 2009). These authors concluded that the X-ray emission associated with IRAS 10214 was either dominated by a dust-enshrouded starburst or that the active nucleus was Compton thick ($\sigma_T \gtrsim 10^{24} \text{ cm}^{-2}$).

The obscured nature of this quasar clearly makes it challenging to disentangle its emission from that of the host galaxy and reliably correct for extinction. In light of these challenges, we carried out VLBI observations which are unaffected by dust extinction and able to isolate high brightness temperature emission originating from an active radio core. Building on the previous multi-wavelength work and incorporating the unique characteristics of VLBI observations, the aims of this paper are threefold:

(i) Detect the obscured active nucleus in a $z \sim 2$ radio quiet quasar and hence estimate its contribution to the total radio flux.

(ii) Use the position to determine the AGN magnification. This is part of a wider case study of this high-redshift galaxy which also aims to quantify the scale of preferential lensing in this system, that is to say, the level of distortion in the spectral energy distribution (SED) that occurs due to different physical emission regions undergoing different magnification boosts. This is important in demonstrating the level of effective ‘chromaticity’ in strong gravitational lensing (due to the background source properties) which affects the physical interpretations of these systems.

(iii) VLBI imaging has the potential to solve a question that arose following the high resolution *HST* imaging (Eisenhardt et al. 1996; Nguyen et al. 1999; Evans et al. 1999): is the UV/optical/NIR arc in this system a single image, or three images that are unresolved with the *HST* spatial resolution? The root cause of this debate stems from the two apparent peaks along the *HST* F814W and *HST* F437M arcs which could be intrinsic source structure (i.e. clumpy UV emission as is typically observed in high-redshift galaxies), or multiple, partially resolved images.

This paper is structured as follows: in §2 and §3 we describe the *EVN* observations and present the results. §4 reviews the ultraviolet polarisation properties of IRAS 10214, while §5 investigates the source-plane position, magnification and multi-wavelength context of the VLBI-detected source. In §6 and §7 we estimate the quasar bolometric luminosity and black hole properties; and close with conclusions in §8. Throughout this paper we assume a concordance cosmology of $\Omega_M = 0.27$, $\Omega_\Lambda = 0.73$, and $H_0 = 71 \text{ km s}^{-1} \text{ Mpc}^{-1}$ (Spergel et al. 2007), which yields an angular size scale of $8.3 \text{ kpc arcsec}^{-1}$ at the redshift of IRAS 10214 ($z = 2.2856$, Ao et al. 2008).

2 OBSERVATIONS

2.1 EVN 1.7 GHz

Observations of IRAS 10214 were made with the *EVN* at 1.66 GHz on 2 and 3 November 2010. Stations that were used in these observations included Jodrell Bank (76-metre), Westerbork Radio Synthesis Array (WRST, phased array), Effelsberg, Onsala (26-metre), Medicina, Torun, Cambridge, Knockin, as well as the three Russian out-stations: Svetloe, Zelenchuk and Badary. This resulted in a baseline coverage of roughly 100 to 5000 km, corresponding to an angular scale range of 500 to 10 mas at an observing frequency of 1.66 GHz. It is for this reason that VLBI observations apply a brightness temperature filter which enables the unambiguous determination of the active core radio flux - one of the primary aims of this work. Observations were carried out with a 1024 Mbit/s recording rate in the standard continuum observing mode, employing eight 16 MHz sub-bands in each hand of polarisation with 2-bit sampling. The total bandwidth of 128 MHz was centred on 1.65899 GHz. Each sub-band was split into 32 channels of 500 kHz

width. The integration period was set to 4 seconds. This results in a time- and bandwidth-smearing limited field-of-view of 0.24 and 0.34 arcmin² respectively. This is based on a metric that measures the angular displacement from the pointing centre at which a 10 percent loss in the response to a point source is measured. These effective fields of view are larger than the optical/IR and molecular extent of IRAS 10214 by two orders of magnitude (**D13b**).

The total duration of the observations was 18 h, of which roughly 70 percent was spent on the target. The observations were split into two 9 h runs that were performed on consecutive days. Given the IRAS 10214 1.7 GHz flux density of $S_{1.7} \sim 1$ mJy, as measured in **D13a**, the phase referencing technique was required. Through a separate EVN calibrator search we selected the $S_{1.7} \sim 70$ mJy source J1027+474 as the best possible phase calibrator for IRAS 10214 given its small angular separation of $\Delta\theta \sim 34$ arcmin. IRAS 10214 was observed for 8 min every 10 min, alternating with the phase calibrator. There was an additional cycle where the standard VLBA phase calibrator (J1027+4803) was observed for 4 min every hour. This was done to monitor the applied phase corrections and to check the resultant astrometric accuracy. 4C39.25 was observed as a fringe-finder. Since the observation was split into 2×9 hr tracks; and the EVN has limited north-south coverage; the resulting beam pattern has a large ripple in the north-south direction (evident in Fig. 1).

Preliminary calibration of the uv-data set was carried out with the EVN automatic pipeline. This pipeline is written in PARSEL-TONGUE (Kettenis et al. 2006), a high-level environment/interface for AIPS, and performs initial fringe-fitting (calibration of delays, rates and phase), and phase and amplitude calibration. The latter are derived from system temperature measurements at individual stations. Following this preliminary calibration, a more detailed, manual calibration is performed in AIPS. This was performed in a cyclic process with detailed data editing, refined delay and rate calibration, as well as phase and amplitude self-calibration on the phase reference sources. Unfortunately, the majority of the observation on the second day was lost due to a combination of circumstances including strong winds, radio frequency interference (RFI), as well as the lack of several stations which did not take part (Effelsberg, Torun).

All imaging was performed with the AIPS IMAGR task with a natural weighting scheme applied to the uv-data. Only after several rounds of the phase and delay calibration cycle (performed on the phase calibrator) did the noise level decrease to $\sigma \sim 23 \mu\text{Jy beam}^{-1}$ for a uv-range limited between 0 - 5 M λ . Including longer baselines (>5 M λ) improves the noise marginally (20 percent) however it results in large and small-scale features that decrease the overall fidelity of the IRAS 10214 map. The reason for this decrease in image quality is due to the fact that the phase calibrator is spatially resolved on the longest baselines, leading to poor phase solutions. For this reason we only consider baselines for which the phase calibrator is clearly unresolved (0 - 5 M λ).

The measured absolute position of the standard VLBA calibrator J1027+4803 is within $\Delta\theta < 0.80$ mas of its cataloged position. This was true for the preliminary pipeline calibration and for the manual delay and self-calibration performed in AIPS. The cataloged position uncertainties are ($\Delta\text{RA} = 0.28$ mas, $\Delta\text{Dec} = 0.43$ mas), sourced from the International Celestial Reference Frame (ICRF-2). These two positions are consistent to within the sub-milliarcsecond level, greatly exceeding the level of accuracy required in this work. The integrated flux density of J1027+4803 ($S_{\text{int}} = 149 \pm 2$ mJy) is consistent with that derived by Helmboldt et al. (2007) with their VLBA 5 GHz observations ($S_{\text{int},5\text{GHz}} = 149.3 \pm$

0.2 mJy). VLBI resolution L-band observations of J1027+4803 have not been performed before prior to this work, so no direct flux density comparison is possible.

In addition, the radio coordinate reference frame must be directly compared to the optical reference frame. This has been performed by Lawrence et al. (1993) who compare the optical and radio positions of 20 compact radio sources in the region around IRAS 10214, however, they do not explicitly state the wavelength at which this comparison is done. They find no significant mean difference, however they note the error on the mean difference is 0.2 arcsec which we take as the systematic uncertainty in the radio-optical reference frame alignment. Greater detail is provided in Lawrence et al. (1993), however, since we use the same data, and our calibrators (as well as the 8 GHz centroids) are consistent, we assume there is an equivalent astrometric matching between radio (1.7 and 8 GHz) and optical reference frames.

3 RESULTS FROM 1.7 GHz VLBI MAP

In Fig. 1 we show the EVN 1.66 GHz CLEANED map with a 9- σ detection. The peak flux density of the imaged data is $S_{\text{peak}} = 209 \pm 23 \mu\text{Jy}$. Fitting a Gaussian to the CLEANED map returns an integrated flux density $S_{\text{int}} = 220 \pm 37 \mu\text{Jy}$, which suggests that the source is unresolved. The measured flux density and position of the detection was checked for a large number of subsets of the data, including splits in frequency, time, and antenna selection. All these tests yield consistent positions and a flux density peak that ranges from $S_{\text{peak}} \sim 190 - 220 \mu\text{Jy}$. The positional uncertainty is $\sigma_{\theta} = 2.2$ mas, which is defined by $\sigma_{\theta} = 0.5 \text{FWHM}/(S/N)$ (Condon 1997).

As shown in Fig. 2, the EVN detection does not appear exactly co-incident with the HST F814W (rest-frame ultraviolet) peaks or the CO (1→0) total intensity map peak. First inspection shows that it lies roughly halfway along the main HST F814W arc (in RA), and > 100 mas northward of the centre of curvature. It is located ~170 mas towards the north-west of the main (eastern) HST F814W peak. As discussed in **D13a**, the HST astrometry is in agreement with determinations from Nguyen et al. (1999); Eisenhardt et al. (1996); Evans et al. (1999) and Simpson et al. (in preparation) to within $\Delta\theta < 10$ mas.

Comparison with HST image-plane configuration

The lensing configuration, detailed in **D13a** and briefly reviewed in §1, includes an arc at near-infrared wavelengths to the south of the lensing galaxy as well as a counter-image towards the north of the lens (see fig. 2, **D13a**). Our EVN observations here do not detect any emission in the region of the HST F814W and HST F160W counter-images. We place a weak, 5- σ limit on the counter-image flux density of $S_{1.7,\text{min}} \lesssim 100 \mu\text{Jy}$ since VLBI detections are generally only considered robust if greater than 5- σ , due to poor uv-coverage¹. We place the same detection limit for any potential emission that is co-located with the secondary CO (1→0) peak (labelled ‘A’ in **D13b**), and for the lensing galaxies identified in **D13a** (Fig. 9). Note that these limits were obtained by shifting the phase centre to the HST F160W centroid in each case.

As stated in §1, one of the questions raised in the past is

¹ Since our uv-coverage is comparatively good for a VLBI observation, 5- σ is a relatively conservative upper limit.

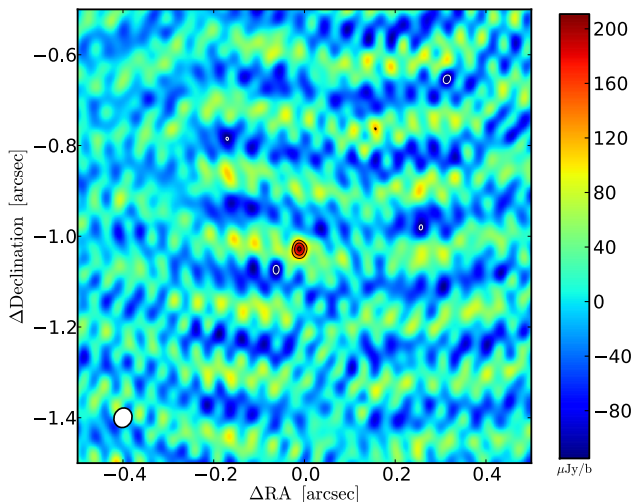


Figure 1. EVN 1.66 GHz continuum map of IRAS 10214. Over-plotted are contours starting from -4 , $4\text{-}\sigma$ and increasing in steps of $2\text{-}\sigma$, where $\sigma = 23 \mu\text{Jy}$ per $44 \times 39 \text{ mas}^2$ beam (white ellipse at bottom left, position angle = -25.1° east of north). The white contours indicate negative contours and black contours are positive. The peak and integrated flux densities are $S_{\text{peak}} = 209 \pm 23 \mu\text{Jy}$ and $S_{\text{int}} = 220 \pm 37 \mu\text{Jy}$. The uv -data are limited to a maximum of $5 \text{ M}\lambda$ based on the quality of the phase solutions derived from the phase calibrator. The observed noise structure results from the EVN synthesised beam. The map co-ordinates are centred on the lensing galaxy *HST* F160W centroid (RA = $10^{\text{h}} 24^{\text{m}} 34.5622^{\text{s}}$, Dec = $47^\circ 09' 10.809''$, see **D13a**)

whether or not the *HST* F814W structure along the arc is intrinsic or if there are multiple images that are convolved together by the *HST* PSF. The *HST* F814W angular resolution was insufficient to unambiguously determine this, however, the higher angular resolution afforded by the EVN will determine if there is a radio core in the proximity of the *HST* F814W emission and more specifically if this radio core has multiple images within the *HST* F814W image plane arc. These VLBI observations will therefore provide further constraints on the lens model, should a detectable radio core be present.

The relative magnification of these three split images would be defined by the cusp relation (e.g. Blandford et al. 1989; Keeton, Gaudi, & Petters 2003), which states that the flux density of the two outer images should have a sum equal to the flux density of the central image. Therefore, if two outer images were present, they should *each* have a flux density of $S_{\text{outer}} \sim 105 \mu\text{Jy}$, equivalent to a $4.5\text{-}\sigma$ detection in the EVN map. No evidence of additional images is present within the extent of the *HST* optical/NIR arc, as illustrated in Fig. 2 which shows the EVN map with overlaid *HST* F814W arc contours. The cusp relation does assume a smooth dark matter profile, however, substructure does not appear to impact image magnification ratios substantially (e.g. McKean et al. 2007; More et al. 2009). Therefore, we assume the EVN image-plane is comprised of a main image (detected here at $9\text{-}\sigma$) and an undetected counter-image that is in the vicinity of the *HST* detected counter-images.

4 ULTRAVIOLET POLARISATION PROPERTIES

Polarisation is a potential consistency check of a lens model, since theoretical arguments show that the polarisation angle undergoes a negligible change in galaxy-scale lensing (i.e. in the weak field

Telescope	Bandpass nm	Polarisation percent	Position Angle degrees	Reference
Keck	412-420	26.5 ± 1.7	69.9 ± 0.2	Goodrich et al. (1996)
Keck	750-800	15.9 ± 0.4	69.9 ± 0.2	Goodrich et al. (1996)
WHT	400-1000	16.4 ± 1.8	75 ± 3	Lawrence et al. (1993)
HST	F437M	28 ± 3	62 ± 2.7	Nguyen et al. (1999)

Table 1. Flux-weighted mean polarisation properties of IRAS 10214 from the literature.

limit, Dyer & Shaver 1992). Since scattered light has a polarisation angle perpendicular to the vector between the source of the photons and the scattering clouds, we would therefore expect the vector between the AGN and scattering cloud(s) to have a position angle $\phi_{\text{pol}} - 90^\circ$, where ϕ_{pol} is the ultraviolet/optical polarisation angle. In this section we collate previous rest-frame ultraviolet polarimetry measurements and review the spatially-resolved *HST* imaging polarimetry reported in Nguyen et al. (1999), before comparing the polarisation with the derived source-plane properties of the EVN detection in §5.

A number of polarisation observations have been performed towards IRAS 10214 (e.g. Lawrence et al. 1993; Goodrich et al. 1996; Nguyen et al. 1999), all of which report high polarisation in the observed optical frame. A review of these results is summarised in Table 1 which shows that the shorter wavelengths have higher polarisation percentages. From the three independent polarisation angles listed in Table 1, we calculate the uncertainty-weighted mean polarisation angle $\bar{\phi}_{\text{pol}} = 68.9 \pm 1.3$ which we use in our analysis of the source plane in §5.

Polarisation angle range

The polarisation angle range reported in Nguyen et al. (1999) is $\Delta\theta_{\text{max}} \sim 100^\circ - 65^\circ = 35^\circ \pm 5^\circ$. A simplified argument is made in Nguyen et al. (1999) that assuming the source of the photons is a point source, and the diameter of the scattering region (D) is known, then the projected distance between the scattering clouds and the photon source can be approximated by the formula $R \approx D \theta_{\text{max}}$. They assumed magnifications of $\mu_{\text{UV}} = 45$ to 250 to derive an intrinsic UV source diameter of $D = 40$ to 100 pc (presumably by dividing the apparent source solid angle by μ_{UV}). This results in an AGN projected distance estimate of $R = 160$ to 65 pc. These magnification estimates were based on the constrained range of arc to counter-image flux ratios (and magnification by proxy). Using the Markov Chain Monte Carlo (MCMC) derived *HST* F814W source-plane diameter of $D = 2 r_s = 720 \pm 180$ pc derived in **D13a**, Sec. 4.1, we find a projected distance to the AGN of $R = 505 \pm 148$ pc. We note however, that this is not a direct comparison since the $\Delta\theta_{\text{max}}$ measurement is made in the *HST* F437M filter, while we have used the *HST* F814W radius. We argue that this is a reasonable approximation, since the arcs in both these filters have very similar lengths (~ 0.7 arcsec) and unresolved widths. However, the *HST* F814W size is possibly an overestimate since the polarised emission is likely to be biased towards the brightest, and therefore more compact emission. Evidence for this claim can be seen in Figure 2 of Nguyen et al. (1999), which shows the extent of the polarised arc to be ~ 0.55 arcsec long, after binning the 0.014 arcsec pixels into 0.042×0.14 arcsec bins. We also note that a more accurate distance may be achieved with a more complex *HST* F814W source model (rather than the circular Gaussian assumed in **D13a**, particularly given the fact that the arc is unresolved in the north-south direction.

The polarisation angle range also provides another important

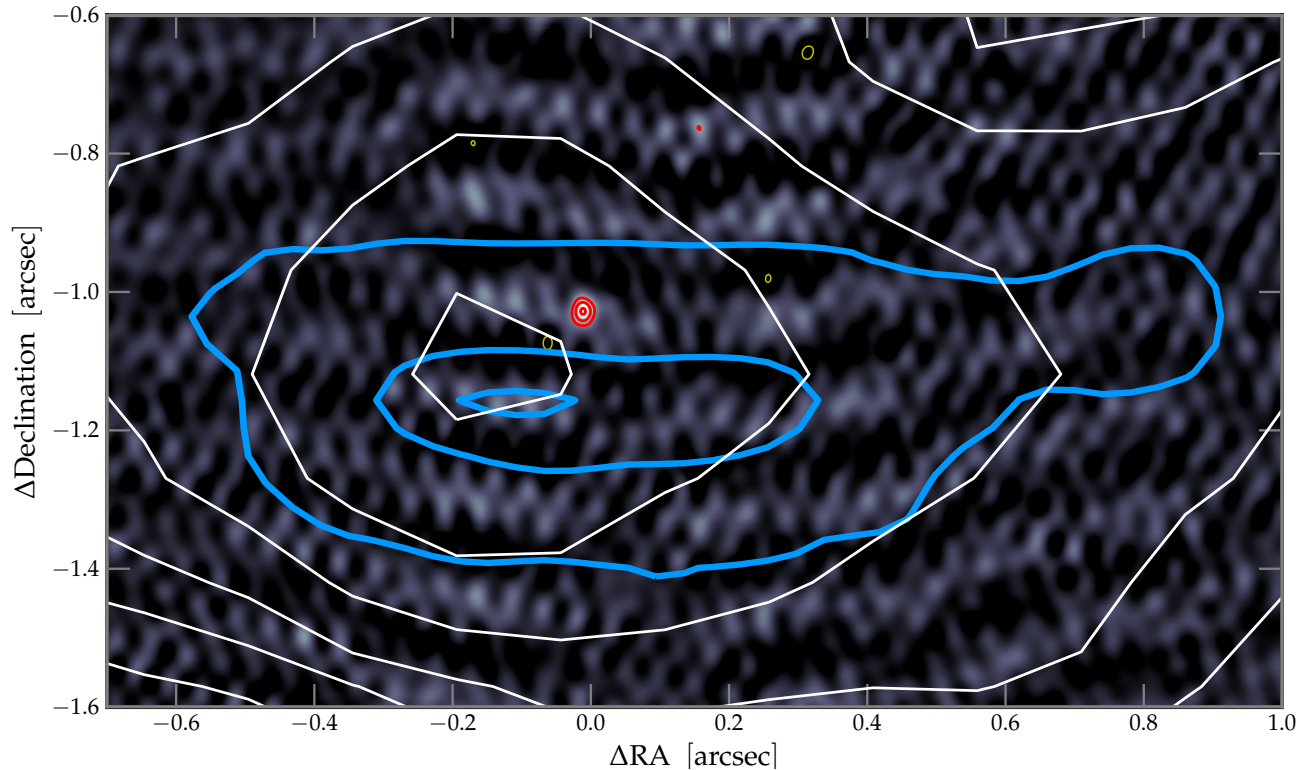


Figure 2. Zoomed-in view of the *EVN* 1.66 GHz continuum map from Fig. 1 with red *positive* contour levels at 4, 6, 8- σ and yellow *negative* contours at -4- σ . The CO(1 \rightarrow 0) total intensity map is over-plotted in white contours with 2- σ intervals that start at -3, 3- σ ($\sigma_{\text{CO}} = 60 \mu\text{Jy beam}^{-1}$). The blue contours show the *HST* F814W (rest-frame UV) arc at 2, 50, 95 percent of the peak flux density. The CO(1 \rightarrow 0) and *HST* F814W point spread functions are ~ 0.7 and 0.1 arcsec respectively. No additional *EVN* images appear to be present within the extent of the *HST* F814W arc.

piece of information. In principle, it enables a robust estimate of the ionisation cone opening angle ($\phi_{\text{cone}} = 0.5 \Delta\theta_{\text{max}} = 17.5^\circ \pm 5^\circ$) assuming the incident photons originate from a point source. The covering factor can therefore be calculated $CF = 0.5 \Delta\theta_{\text{max}} / (\pi/2) = 0.195 \pm 0.028$ by spherical symmetry. We use this observational constraint in our bolometric luminosity estimates in §7.

5 SOURCE PLANE

We calculate the source-plane position of the *EVN* detection using the *GLAMROC*² software. We use Lens Model A, as defined in **D13a**. This assumes a Singular Isothermal Ellipsoid (SIE) potential for the main lens at $z = 0.893$, and a Singular Isothermal Sphere (SIS) potential for the secondary, line-of-sight galaxy at $z = 0.782$. IRAS 10214 is assumed to be a point source, which is consistent with the Gaussian fit presented in §3. The *EVN* source-plane co-ordinates are therefore the two remaining free parameters to solve for. We perform ray-tracing of a point source from the source plane to the image plane, and minimise the predicted image-plane position with respect to the measured *EVN* position. The resultant magnification of the best-fit point-source model is $\mu_{\text{EVN}} = 68$. The magnification random error due to the ~ 2 mas *EVN* positional uncertainty is of order 5 percent (derived by adding a 2 mas dispersion to the trial model position prior to ray-tracing), and therefore the systematic uncertainty of ~ 40 percent discussed

in **D13a** (Sec. 3.5) dominates the absolute magnification uncertainty. The *EVN* 1.7 GHz component magnification is therefore $\mu_{\text{EVN}} = 68 \pm 3(\pm 27)$, where the systematic uncertainty is enclosed in parentheses. The *EVN* source-plane position is shown in Fig. 3.

Given the low probability that a small (< 50 mas) source is located within < 20 mas from the cusp of our lens model, we describe a number of consistency checks on the *EVN* source-plane position, and its high magnification. Firstly, the *EVN* source is northward of the *HST* UV/optical arcs as stated in §3; and does not split into 3 images (at 4.5- σ significance, see §3); therefore it is most likely to the south of (or on) the cusp of the caustic. Secondly, the *EVN* detection is positioned roughly along the vector that extends from the centre of the lens and bisects the angle subtended by the rest-frame UV/optical arcs. This implies that the source-plane position must be very close ($< \text{few milli-arcseconds}$) to the cusp of the caustic, since this is a region with large tangential deflection angles. The *EVN* point source is therefore essentially ‘wedged’ between the inner-caustic and the *HST* UV/optical arc, which will always result in high magnifications regardless of changes in the macroscopic lens model. In Fig. 4, we plot the predicted total magnification as a function of intrinsic source radius, assuming the source is centered on the *EVN* source plane position.

Assuming the *EVN* point source is the obscured active nucleus, then its source-plane position is consistent with a number of multi-wavelength observations outlined below.

(i) Simpson et al. (in preparation) present two narrow-band maps centred on the redshifted C IV and [O III] lines, which are typical broad-line and narrow-line region emission lines respectively.

² Gravitational Lens Adaptive Mesh Raytracing of Catastrophes, see <http://kipac.stanford.edu/collab/research/lensing/glamroc>

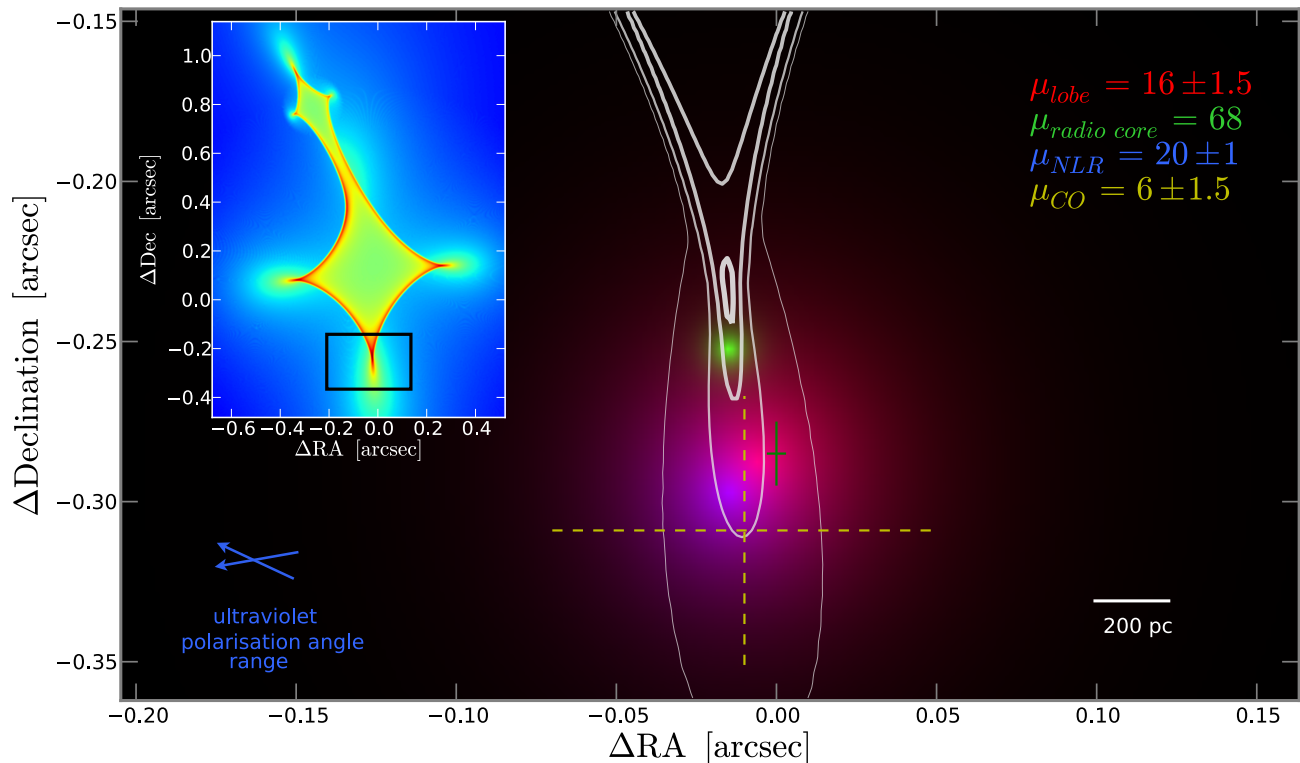


Figure 3. Source plane reconstruction of IRAS 10214 showing the radio core (green, *EVN* 1.7 GHz), scattered quasar light (blue, *HST* F814W) and radio lobe (red, *MERLIN* 1.7 GHz). The yellow, dashed cross shows the CO (1→0) total intensity map source-plane centroid and its uncertainty (the extent of the source-plane CO (1→0) component is beyond this entire frame). The green cross indicates the 8 GHz map source-plane centroid and its uncertainty. The white contours represent lines of equal magnification extending from the caustic at levels $\mu = 10, 20, 50, 100$. The blue arrows (bottom left) depict the range of UV polarisation angles along the *HST* F437M arc. The inset shows the full lens caustic with colour-scale representing magnification and the black rectangle showing the borders of the enlarged region.

They determine the centres of curvature of both and find that the C iv arc is roughly 50 ± 20 mas northward of the [O iii] centre of curvature for the highest S/N bins. At face value this implies that the BLR (or scattered BLR light) is northward of the NLR, which in our **D13a** model is one-sided. This is consistent with resolved NLR imaging performed in the local Universe (Liu & Pooley 1991; Simpson et al. 1997) and implies that the active nucleus is northward of the NLR and *HST* F814W centers of curvature. The relative configuration of the emission associated with the BLR and NLR is therefore consistent with the source-plane *EVN* position, if it traces an obscured active nucleus.

(ii) Comparison of the source-plane ultraviolet and radio core positions shows that the median ultraviolet polarisation angle ($\langle \phi_{\text{pol}} \rangle = 82.5^\circ \pm 5^\circ$, with a range $\sim 65^\circ - 100^\circ$) is roughly perpendicular to the vector connecting the *EVN* radio core and *HST* F814W source-plane centroids ($\phi_{\text{core,uv}} \sim 0^\circ$). This supports the view that the *EVN* detection is the dust-embedded source that emits the scattered, and therefore polarised, ultraviolet/optical radiation.

(iii) The lensing inversion predicts that the *EVN* and *HST* F814W source-plane centroids are separated by a distance $R = 370 \pm 148$ pc, where the uncertainty is dominated by the absolute magnification uncertainty. As calculated in Sec. 4, the projected distance between the AGN and the scattered ultraviolet light is $R = 505 \pm 145$ pc, which is based on the ultraviolet polarisation angle range ($\Delta\theta_{\text{max}} = 35 \pm 5^\circ$) and the predicted *HST* F814W source-plane radius ($r_s = 360 \pm 90$ pc). The two independently calculated

projected distances between *EVN* and *HST* F814W source-plane centroids are therefore consistent with one another.

The lensing inversion places the *EVN*-detected radio core at a position qualitatively consistent with the Nguyen et al. (1999) prediction of the AGN position. This is a promising example of the potential held by high sensitivity, high resolution spectro-polarimetry with next generation 30-40 metre optical/IR telescopes in accurately locating the obscured active nuclei in high-redshift galaxies.

6 DISCUSSION

6.1 AGN Core or Highly-Magnified Star-Formation Clump?

At first glance, the *EVN* detection is likely to be the AGN radio core, however, careful consideration is required given the close proximity of the cusp of the caustic. IRAS 10214 was discovered at $\lambda_{\text{obs}} = 100 \mu\text{m}$, a wavelength biased towards warm, partially AGN-heated ($T \sim 100$ K) dust. This is consistent with its AGN features across the spectrum and so the close proximity of an AGN core to the cusp would be expected. However, the probability that such a compact point source is within a few milli-arcseconds of the cusp is low. We must consider an alternative scenario where the *EVN* detection is co-spatial with a star-forming complex with an exceptionally large magnification ($\mu > 100$). This potentially has a higher probability, given the supernovae rate we expect from the large star formation rate (SFR) in IRAS 10214 ($SFR > 100 M_\odot \text{yr}^{-1}$) and therefore the number of star-formation clumps.

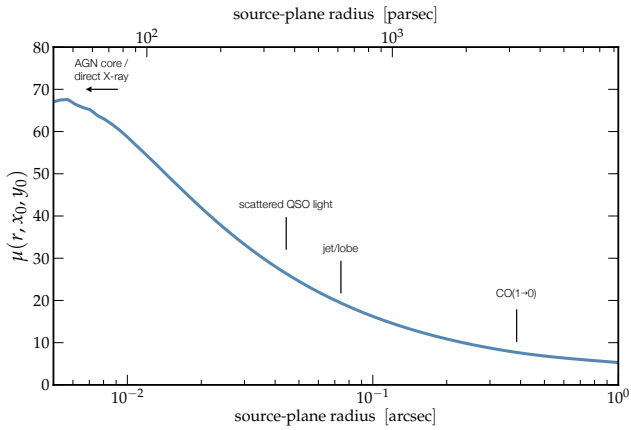


Figure 4. Total magnification as a function of source-plane scale radius, assuming the EVN source-plane centroid. The annotations serve as a rough guide of the physical sizes. The centroids of the listed components are not the same as the EVN component and therefore the resultant magnifications are marginally different. The point source magnification at the best-fit EVN position is $\mu_{\text{EVN}} = 68$.

We calculate the brightness temperature of the EVN -detected emission using Equ. 6 in **D13a**. We assume a solid angle equal to the area of the beam effective radius (i.e. $\Omega_{\text{beam}} = \pi \frac{1}{2} \theta_{\text{maj}} \frac{1}{2} \theta_{\text{min}}$ where $\theta_{\text{maj, min}}$ are the FWHM values of the beam). The peak flux density is $S(\nu_0) = S_{\text{peak}} = 209 \mu\text{Jy}$, which results in a rest-frame 5.45 GHz brightness temperature lower limit of $T_{\text{B}} > 5 \times 10^5 \text{ K}$, since the source is unresolved. This lower limit seems to rule out a significant contribution from star formation, which appears to saturate at $T_{\text{SF}}^{\text{max}} \sim 10^5 \text{ K}$ (Muxlow et al. 1994). Note that these calculation do not depend on the magnification as the surface brightness, and hence the brightness temperature, are not affected by gravitational lensing.

More distinguishing is the implied SFR density (Σ_{SFR}) if we assume that the EVN -detected flux density is associated with star formation. Using Equ. 7 in **D13a**, we calculate the implied SFR assuming all the emission is due to star formation. We assume a 1.7 GHz flux density $S_{\text{peak}} = 209 \mu\text{Jy}$, a spectral index $\alpha = 0.8$ and set the intrinsic source size equal to the EVN 1.7 GHz beam. This results in a lower limit of $\Sigma_{\text{SFR}} > 8.4 \times 10^4 \text{ M}_{\odot} \text{ yr}^{-1} \text{ kpc}^{-2}$. This is significantly larger than the theoretically motivated and observationally supported value of $\Sigma_{\text{SFR}}^{\text{max}} \sim 1000 \text{ M}_{\odot} \text{ yr}^{-1} \text{ kpc}^{-2}$ (see Elmegreen 1999; Thompson, Quataert, & Murray 2005; Scoville, Yun, & Bryant 1997; Downes & Solomon 1998). These arguments, in addition to those presented in §5, appear to support that this is an AGN core, which is what we assume for the remainder of the paper. As argued in §5, this is consistent with a number of multi-wavelength and rest-frame ultraviolet polarisation properties.

6.2 Nature of VLA 8 GHz Map Peak

In **D13a**, we suggested that the VLA 8 GHz map could potentially be dominated by a radio core, based on the radio spectral index behavior from 330 MHz through 16 GHz. However, the 8 GHz centroid is significantly offset from the EVN detection presented here (see Fig. 5), with a separation of $\Delta\theta \sim 300 \pm 20(\pm 200) \text{ mas}$, where the first uncertainty is the quadrature sum of the two random position uncertainties (8 GHz discussed in **D13a**), and the second uncertainty in parentheses is the systematic uncertainty based on the radio-optical reference frame alignment. The nature of the 8 GHz

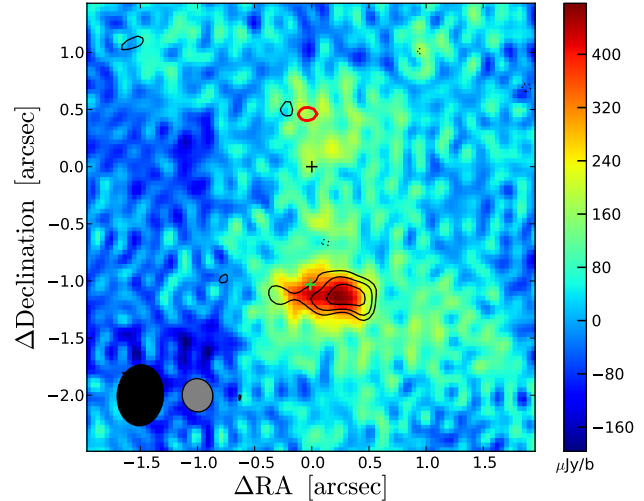


Figure 5. MERLIN 1.7 GHz map shown in colour-scale with $\sigma \sim 46 \mu\text{Jy}$ per $405 \times 349 \text{ mas}^2$ beam (position angle = -4.35°). Over-plotted in black contours is the 8 GHz VLA map with $\sigma \sim 11 \mu\text{Jy}$ per $292 \times 267 \text{ mas}^2$ beam (position angle = -79.64°). Contours are at $\pm 3\sigma$ and increase by a factor of $\sqrt{2}$. Dashed lines represent the negative contours. The MERLIN and VLA beams are illustrated in the bottom left corner as black and grey ellipses respectively. The green cross indicates the location of the EVN detected radio core, where the cross length is a factor $\gtrsim 10$ larger than the EVN positional uncertainty. The red ellipse towards the north is the HST F814W counter-image contour. The black cross indicates the Sersic-fitted centroid of the lensing galaxy as measured from the HST F160W map

emission is puzzling, since we would expect it to be co-located with the EVN detection, especially since their flux densities are very similar ($S_{8\text{GHz}} = 280 \mu\text{Jy}$), assuming a flat radio spectrum. It does not seem that this discrepancy can be discarded on the basis of insufficient astrometric accuracy. This is because the 8 GHz centroid was measured for two independent observations performed in 1991 and 1995, both with the VLA in A-configuration and hence a resolution of $\theta_{\text{syn}} \sim 0.23 \text{ arcsec}$. As discussed in §2.1, the astrometry of the EVN map appears secure to within $\lesssim 2 \text{ mas}$. The true nature and extent of the 8 GHz emission will be further probed by a C-band JVLA polarisation observation of IRAS 10214 in A-configuration ($\sim 30 \text{ mas}$ angular resolution) with 2 GHz bandwidth. With the EVN map we can estimate a $5\text{-}\sigma$ limit on the spectral index of the 8 GHz peak of $\alpha < -0.54$, assuming it is a point source and defining $\alpha \equiv -\log(S_1/S_2)/\log(\nu_1/\nu_2)$.

6.3 Resolved Out Radio Emission

The radio core flux is ~ 20 percent of the total flux in the 1.7 GHz MERLIN map presented in **D13a**. If we assume the remaining flux is associated with star formation and a spectral index $\alpha = 0.8$, the implied star formation rate is $SFR \sim 3.2 \times 10^4 \mu^{-1} \text{ M}_{\odot} \text{ yr}^{-1}$ following Equ. 7 in **D13a**. If the MERLIN 1.7 GHz magnification ($\mu_{1.7} = 16 \pm 1.5$) derived in **D13a** is assumed to be equivalent to the star formation magnification, then this results in an intrinsic star formation rate of $SFR \sim 2 \times 10^3 \text{ M}_{\odot} \text{ yr}^{-1}$. This is an exceptional star formation rate, which suggests that there may be significant flux in the radio jet/lobe components that are resolved out by the EVN observations. It is unlikely that the total magnification boost of the star formation emission region is higher, since any disk with a reasonable star formation size ($\gtrsim 1 \text{ kpc}$) undergoes a magnification boost of $\mu \lesssim 10$.

7 QUASAR BOLOMETRIC LUMINOSITY

Having detected the radio core and made an estimate of its magnification, we now wish to use these results to estimate the quasar bolometric luminosity in IRAS 10214 using five methods in the X-ray, ultraviolet and mid-infrared

7.1 [O III] Equivalent Width L_{bol} Estimate

The first method uses the equivalent width (EW) of the forbidden [O III] λ 5007 line to measure the ‘missing’ optical continuum flux as a result of the obscuring geometry (Miller et al. 1992). Their method measures the average [O III] equivalent width of 76 type-I quasars from the Bright Quasar Survey (BQS), which provides a way to estimate the obscured AGN continuum flux, and hence the extinction. The idea is that the narrow-line-region flux will be largely unaffected by the orientation of the quasar since it is above and beyond the putative torus, whereas the central AGN continuum would be obscured under the unified quasar model (Antonucci 1993). Since the equivalent width measures the fraction of energy of a spectral line relative to the underlying continuum, the greater the central AGN obscuration, the more exaggerated the equivalent width of a narrow line like [O III] will be from its intrinsic value.

Miller et al. (1992) measure an average rest-frame [O III] equivalent width $\langle EW \rangle_{\text{OIII}} = 24 \pm_{12}^{25} \text{ \AA}$ for their BQS survey sample. Serjeant et al. (1998) measure the [O III] rest-frame EW of IRAS 10214 to be $EW_{\text{OIII}} = 580 (1+z)^{-1} = 176 \text{ \AA}$. Two approaches can now be followed to estimate the bolometric luminosity. The first simply assumes that given a measurement of the [O III] line flux density, one can estimate the bolometric luminosity with the relation

$$L_{\text{bol,OIII}^1} = L_{\text{OIII}} \mu_{\text{NLR}}^{-1} BC, \quad (1)$$

where $L_{\text{OIII}} = 2.05 \times 10^{37} \text{ W}$ (Serjeant et al. 1998; Lacy, Rawlings, & Serjeant 1998), $\mu_{\text{NLR}} = 20 \pm 1$ is the NLR magnification derived in **D13a** from the *HST* F814W map, $BC = 89.9$ is a bolometric correction factor calculated from the average quasar [O III] equivalent width (Miller et al. 1992) and a correction factor to convert the specific luminosity at 5100 \AA to a bolometric luminosity (Elvis et al. 1994). This results in a bolometric luminosity estimate of $L_{\text{bol,OIII}^1} = 2.4 \pm 0.6 \times 10^{11} L_{\odot}$.

The second estimate, $L_{\text{bol,OIII}^2}$, is less direct. It extrapolates an optical continuum flux based on a dust-reddened quasar SED fit to the ultraviolet flux data points. Scattered QSO light is presumed to dominate the latter. By comparison of the observed IRAS 10214 and average quasar [O III] equivalent widths, the argument can be made that only $13.6 \pm_{6.8}^{14}$ percent of the AGN core continuum emission is observed at 5100 \AA . This is calculated by taking the ratio of $EW'_{\text{OIII}}/\langle EW \rangle_{\text{OIII}}$, where EW'_{OIII} is the measured [O III] equivalent width; $\langle EW \rangle_{\text{OIII}}$ is the average [O III] equivalent width (Miller et al. 1992). Therefore, we can estimate the true specific luminosity at 5100 \AA as follows:

$$\begin{aligned} L_{5100,\text{true}} &= L'_{5100,\text{obs}} \frac{EW'_{\text{OIII}}}{\langle EW \rangle_{\text{OIII}}} \\ &= L_{5100,\text{obs}} \mu_{5100}^{-1} \frac{EW_{\text{OIII}}}{\langle EW \rangle_{\text{OIII}}} \frac{\mu_{5100}}{\mu_{\text{NLR}}}, \end{aligned} \quad (2)$$

where $L'_{5100,\text{obs}}$ is inferred from the lensed, host-galaxy-reddened quasar flux density at 5100 \AA ; $L'_{5100,\text{obs}} = 1.9 \times 10^{23} \text{ WHz}^{-1}$; $\mu_{5100}/\mu_{\text{NLR}}$ accounts for the difference in magnification between the

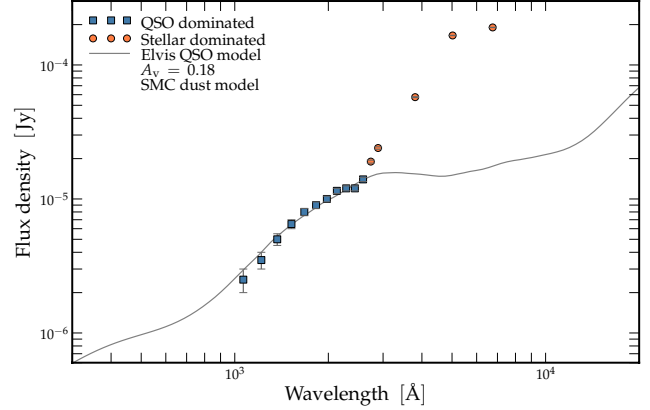


Figure 6. Ultraviolet fit to a reddened quasar model. The dust extinction model is from Pei (1992) and the intrinsic quasar model is an average from the sample of Elvis et al. (1994). Only the blue squares are included in the fit as these are presumed to be dominated by scattered quasar light, as suggested by the high degree of polarisation. We argue that orange circles are dominated by the host galaxy’s stellar component which is supported by the lower magnification seen at rest-frame optical/NIR wavelengths (as surmised from lower arc to counter-image flux ratios).

narrow-line region and the AGN nucleus, and EW_{OIII} is the equivalent width in the absence of differential lensing effects. Note that $\mu_{5100} = \mu_{\text{AGN}}$ since we are interested in the specific luminosity of the quasar at 5100 \AA .

To calculate $L'_{5100,\text{obs}}$, we fit the average quasar spectrum (Elvis et al. 1994) to the 11 UV photometric points between rest-frame 1000 – 2750 \AA and extrapolate to 5100 \AA since this wavelength is dominated by stellar emission as discussed in **D13a** and §8.2. This includes the *HST* F814W photometric point and is therefore assumed to be scattered quasar emission given the high degree of polarisation. The UV photometric points are reddened by a range of dust models from Pei (1992) to account for *host galaxy* extinction, since this is scattered QSO light. The fit results in a best-fit visual extinction $A_v = 0.18$ with a Small Magellanic Cloud (SMC) dust grain model, with a $\chi^2 = 1.3$. The extinction is comparable to the $A_v \sim 0.3$ from Lacy, Rawlings, & Serjeant (1998) toward the NLR based on the He II 468.6 / 164.0 ratio of 4.3). The best fit extinction, bolometric luminosity, and χ^2 have very little variance with subsets of the UV photometric points (from 4 to 11), however the goodness-of-fit begins to decrease substantially once the optical photometry is included, as one would expect with a significant stellar component. The full resolution UV spectrum from which these photometry points originate from, has a continuum baseline that Rowan-Robinson et al. (1993) fit with two linear models which meet at $\lambda_{\text{rest}} \sim 2600 \text{ \AA}$. This supports our selection of fitting boundaries, as well as the goodness of fit behaviour as this boundary is extended into optical wavelengths. The reddened quasar fit to the observed ultraviolet spectrum is plotted in Fig. 6.

This implies a bolometric luminosity $L_{\text{bol,OIII}^2} = 1.9 \pm_{1.0}^{2.0} \times 10^{39} \mu_{5100}^{-1} \mu_{5100} \mu_{\text{NLR}} \text{ W}$, since $L_{5100,\text{true}} = L_{\text{OIII}}/(24 \pm_{12}^{25})$ as determined for unobscured quasars in Miller et al. (1992). Assuming our previously derived magnification factors, this leads to a $L_{\text{bol,OIII}^2} = 2.8 \pm_{1.4}^{2.8} \times 10^{11} L_{\odot}$, which is 16 percent greater than the first $L_{\text{bol,OIII}^1}$ method. We adopt the average of the two and note that the uncertainty is dominated by $\langle EW \rangle_{\text{OIII}}$ scatter. The result is $L_{\text{bol,OIII}} = 2.6 \pm_{1.3}^{2.6} \times 10^{11} L_{\odot}$.

7.2 Ultraviolet L_{bol} Estimate

The scattered quasar light we observe is of course a fraction of the total quasar light. If we can determine the covering factor and appropriate magnification, then we can determine the intrinsic quasar bolometric luminosity. The magnification is reasonably assumed to be $\mu_{\text{NLR}} = 20 \pm 1$ since the *HST* F814W observation directly probes the emission assumed to be dominated by the scattered quasar light. The covering factor ($CF = 0.195 \pm 0.028$) is approximated by the maximum change in polarisation angle ($\Delta\theta_{\text{max}}$) of the scattered ultraviolet light as discussed in §4. The luminosity at 2400 Å (rest-frame *HST* F814W) is $\nu L_{2400} = 5 \pm 2 \times 10^{11} L_{\odot}$. We also account for host galaxy extinction ($A_V = 0.18$) based on the modeling described in §7.1. This leads to a UV bolometric luminosity estimate of $L_{\text{bol,UV}} = L_{2400} BC_{2400\text{Å}} 10^{A_V/2.5} / \mu_{\text{NLR}} = 2.7 \pm 1.1 \times 10^{11} f_{\text{scatt}}^{-1} L_{\odot}$. The scattering fraction f_{scatt} , which is poorly constrained, will increase the derived value if much smaller than unity. We are fairly ignorant of the true f_{scatt} value, and plot the $L_{\text{bol,UV}}$ estimate in Fig. 8 (green line) assuming $f_{\text{scatt}} = 100$ percent.

7.3 Mid-Infrared L_{bol} Estimates

Spitzer mid-infrared spectroscopy has proved a powerful technique to probe the heart of quasar host galaxies through dust heating and spectral features. In the case of IRAS 10214, the mid-IR spectrum is best fit with three components: (1) a typical star-forming dust temperature of 50 K; (2) a warm 210 K component; (3) a hot 600 K component (see Teplitz et al. 2006; Efstathiou 2006). We motivate appropriate covering factors and magnifications for the latter two components which we expect are predominately heated by the central AGN. This will allow additional estimates of the intrinsic bolometric luminosity.

600 K Dust

Efstathiou (2006) fit a 600 K component to the mid-IR spectrum that has an apparent bolometric luminosity $L_{\text{bol,600K}} = 7.4 \times 10^{11} L_{\odot} CF_{600\text{K}}^{-1} \mu_{600\text{K}}^{-1}$. The covering factor ($CF_{600\text{K}}$) and magnification ($\mu_{600\text{K}}^{-1}$) at this temperature do not represent that of a distinct physical component, but rather a representative average of the hot dust component. We contend that this ‘component’ is located within ~ 50 pc of the radio core and therefore has a mean magnification of $\mu_{600\text{K}} \sim 68$, as inferred from Fig. 4. The distance limit is based on mid-IR interferometric (using VLTI) size limits from nearby Seyfert galaxies (Tristram et al. 2009; Tristram & Schartmann 2011). These authors find a size-luminosity relation $s = p L^{0.5}$, where $p = 1.8 \pm 0.3 \times 10^{-18} [\text{pc W}^{-0.5}]$. This implies a torus size of order $s = 30 - 55$ pc for IRAS 10214 for range of quasar bolometric luminosities determined for $L_{\text{bol,UV}}$ and $L_{\text{bol,OIII}}$. The covering factor for this component is set to the value derived in Mor, Netzer, & Elitzur (2009), who model the mid-IR spectra of 26 luminous QSOs with 3 dust components: (1) a clumpy torus; (2) a dusty narrow line region; (3) a hot blackbody representing the hottest dust around the nucleus. A 600 K dust component would clearly be associated with the last of these three components, for which the authors find a mean covering factor $\langle CF \rangle = 0.23 \pm 0.1$. This covering factor compares well with our adopted value $CF = 0.195 \pm 0.028$ which is based on the maximum change in polarisation angle. Based on the polarisation-determined covering factor and magnification we estimate a bolometric luminosity $L_{\text{bol,600K}} = 4.8 \pm_{2.2}^3 \times 10^{10} L_{\odot}$.

210 K Dust

This bolometric luminosity estimate follows the same reasoning as the 600 K component, however the average distance of clouds contributing to this temperature is greater than that of the hotter, 600 K dust and therefore likely to undergo a different amplification boost. The peak rest wavelength of this component is $14 \mu\text{m}$, just longward of the $10 \mu\text{m}$ silicate feature. Based on evidence from silicate emission in type II Seyferts (e.g. Sturm et al. 2006; Shi et al. 2006), as well as resolved silicate imaging on ~ 100 pc scales (Schweitzer et al. 2007), it appears that the $\sim 10 \mu\text{m}$ emission may be dominated by a combination of outer torus and NLR dust cloud emission. Following the multi-component mid-infrared modelling of Mor, Netzer, & Elitzur (2009) who find a correlation between NLR cloud distance and bolometric luminosity, we estimate a NLR distance of $r_{\text{NLR}} = 125 \pm_{25}^{35}$ pc based on the range of values derived for $L_{\text{bol,UV}}$ and $L_{\text{bol,OIII}}$.

We make the simplified argument that the 210 K component has a 125 pc radius; the same covering factor as derived before ($CF = 0.195 \pm 0.028$); and is centred on the EVN point source which results in a magnification $\mu_{210\text{K}} \sim 50$ (from Fig. 4). Efstathiou (2006) and Teplitz et al. (2006) find a 210 K component bolometric luminosity of roughly $L_{\text{bol,210K}} = 5.5 \times 10^{12} L_{\odot} CF_{210\text{K}}^{-1} \mu_{210\text{K}}^{-1}$. We therefore find $L_{\text{bol,210K}} = 5.6 \pm 3 \times 10^{11} L_{\odot}$ from the assumptions above. This is higher than the other bolometric estimates, especially that based on the 600 K dust. This could be expected since some, potentially large, fraction of the 210 K dust heating will arise from the prodigious star formation in IRAS 10214. An estimate of this contribution is the fraction of luminosity a 80 K greybody (i.e. dust primarily heated by star formation; and roughly where the IRAS 10214 mid-IR spectrum peaks) contributes at $\lambda = 14 \mu\text{m}$, the wavelength that corresponds to the peak of a 210 K greybody. The 80 K component contributes 1.5 percent assuming equal peak luminosities for the two temperature components. Previous work has shown that the star formation dominates the bolometric luminosity of IRAS 10214 at the >90 percent level (e.g. Rowan-Robinson et al. 1991; Teplitz et al. 2006; Efstathiou 2006). If we assume a star formation to quasar L_{bol} ratio in the 90-95 percent range, then an 80 K greybody contributes ~ 15 -30 percent to the flux at $14 \mu\text{m}$ (210 K peak wavelength). This suggests the $L_{\text{bol,210K}}$ estimate is significantly contaminated by star formation.

7.4 X-ray L_{bol} Estimate

This method uses an X-ray spectrum fit employing the models of Wilman & Fabian (1999) to find the best-fit column density of intervening hydrogen (N_{H}). The X-ray models are Monte Carlo derived and assume an intrinsic unobscured type-I quasar X-ray spectrum of the form $L_{\nu} \propto \nu^{-0.9} e^{-\nu/\nu_c}$ (where $h\nu_c = 360$ keV) as described in Madau, Ghisellini, & Fabian (1994). Wilman & Fabian (1999) generated a library of models with a range of hydrogen column densities (N_{H}), assuming $5 \times$ solar metallicity as they find this provides a superior fit to the hard X-ray background which peaks at ~ 30 keV. The models further assume a 2 percent flux component that is scattered off the central ionized medium. For simplicity, we do not consider models that include a reflection component off an accretion disk. In our MCMC routine we include a dispersion on the scattered percentage with FWHM = 10 percent (in the range 0 – 100 percent). Although Wilman & Fabian (1999) assume a fixed scattering fraction, we wish to decrease the sensitivity to this assumption, particularly as they note that there is likely some dis-

persion in this quantity, as suggested by high infrared luminosity ($L \gtrsim 10^{13} L_{\odot}$) IRAS galaxies observed with the ROSAT High Resolution Imager (HRI), that place upper limits on the 0.1 ± 2.4 keV fluxes and imply scattering fractions below ~ 0.5 per cent (Fabian et al. 1996; Wilman et al. 1998). While the selection of a 10 percent dispersion FWHM for our MCMC chains is relatively arbitrary, it gives practically the same probability to the lower values for luminous infrared galaxies reported above, whilst also opening up the parameter space to incorporate the effect of higher values.

The resulting models are compared to the X-ray observations of IRAS 10214 with both Chandra and XMM-Newton Space Telescopes (which have consistent, albeit low S/N, results). Samples of the posterior probability distribution function (PDF) of the hydrogen column density N_{H} and bolometric luminosity L_{bol} are drawn in a MCMC algorithm similar to that described in **D13a**. Fitting a library of X-ray models to the three X-ray data points is a weakly-constrained problem, and so an important caveat to these results is that we assume a hydrogen column density prior N_{H} with a mean of 10^{24} cm^{-2} and a logarithmic FWHM of 2 dex. This is based on the evidence presented by Alexander et al. (2005) that IRAS 10214's nucleus must be Compton-thick ($N_{\text{H}} > 1.5 \times 10^{24} \text{ cm}^{-2}$). They find the measured X-ray luminosity is 1-2 dex lower than expected given the measured [O III] line strength and the $L_{[\text{OIII}]} - L_{\text{X}}$ correlation (e.g. Netzer et al. 2006). If the obscuring gas column density is significantly larger than $N_{\text{H}} \sim 10^{25} \text{ cm}^{-2}$ then our assumption breaks down and the bolometric luminosity derived here is likely to be too low. However, if one assumes the X-ray luminosity is dominated by the AGN (and not less-obscured star formation) then the L_{OIII} shows that the hydrogen column density cannot be significantly larger than 10^{25} cm^{-2} (Alexander et al. 2005). Note that if the narrow line region (and hence [O III] λ 5007 flux) has a lower magnification factor than the active nucleus, as predicted by our lens model, this will increase the $L_{[\text{OIII}]} - L_{\text{X}}$ discrepancy, yielding greater evidence that the active nucleus is Compton-thick.

Under these assumptions, we find $\log(N_{\text{H}}) = 23.5 \pm_{0.2}^{0.4} \text{ cm}^{-2}$ from the MCMC spectral fit illustrated in Fig. 8. By comparison with the model type-I X-ray spectrum we can estimate the intrinsic X-ray luminosity of IRAS 10214 and therefore the intrinsic bolometric luminosity. We find $L_{\text{bol,Xray}} = 1.3 \pm_{0.7}^{1.2} \times 10^{39} \mu_{\text{X}}^{-1} \text{ W}$ ($3.4 \times 10^{12} \mu_{\text{X}}^{-1} L_{\odot}$), where μ_{X} is the magnification of the X-rays emanating from the AGN core. We do not have a strong constraint on the magnification of this unresolved X-ray detection given its low S/N and the absolute astrometric accuracy of Chandra ($3\sigma = 0.8 \text{ arcsec}$)³, however, as an indicative estimate, we assume that $\mu_{\text{X}} = \mu_{\text{EVN}}$, which yields an intrinsic bolometric estimate $L_{\text{bol,X}} = 5.3 \pm_{3.0}^{5.1} \times 10^{10} L_{\odot}$. We emphasise that this X-ray magnification could vary substantially from the assumed magnification since micro-lensing is observed in X-ray emitting regions of AGN (e.g. Pooley et al. 2007; Chen et al. 2012), but not frequently in the radio emitting region (e.g. Koopmans et al. 2003), suggesting that the former are constrained to smaller regions than the latter. However, co-spatial regions smaller than the VLBI core will tend to a magnification of $\mu_{\text{X}} \sim \mu_{\text{EVN}} \sim 68$.

The 20-30 ks observations here combined with the magnification ($\mu \sim 68$) make this almost equivalent to the most sensitive X-ray field ever observed (Chandra Deep Field South, 4 Ms), however the lack of spectral resolution results in large degeneracies (particularly due to the scattering fraction) which are overcome to

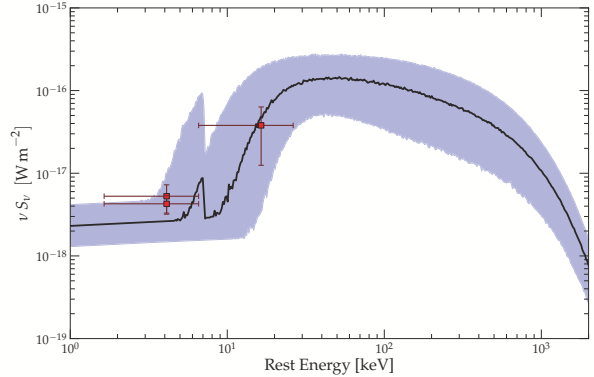


Figure 7. Best-fit X-ray model spectrum to the Chandra and XMM-Newton space telescopes. The shaded region corresponds the 68 percent confidence levels of the hydrogen column density (N_{H}) and quasar bolometric luminosity (L_{bol}). The bands correspond to 0.5-2 keV and 2-8 keV.

some extent with our assumed priors. Further progress will only be achieved with greater depth and spectral coverage/resolution.

7.5 Bolometric luminosity of IRAS 10214

In Fig. 8 we show the 2D posterior PDF of the X-ray derived hydrogen column density (N_{H}) and bolometric luminosity, which illustrates the degeneracy between these two parameters (below the Compton Limit). Over-plotted are two dashed red lines that indicate the two dust bolometric luminosity estimates. The blue horizontal line and shading indicate the $L_{\text{bol,OIII}}$ estimate along with its 68 percent confidence levels. Finally, the green dashed line shows the estimate based on the scattered quasar light. While the uncertainty is large in all of the above methods ($\sim 0.3 - 0.5$ dex), they all show a reasonably consistent picture of a hidden quasar with intermediate luminosity. Furthermore, our highest estimate is the that which we expect to be most contaminated by star formation (i.e. the 210 K dust bolometric luminosity estimate).

The five methods here are based on high-exposure space telescope observations and so it is challenging to see where we will make substantial progress in determining the bolometric luminosity of obscured quasars like IRAS 10214 before the next generation of telescopes or extended, dedicated programmes with current facilities. We adopt a quasar bolometric luminosity that is the weighted mean of the five methods presented here, which results in a value of $\log_{10}(\langle L_{\text{bol,QSO}} \rangle / L_{\odot}) = 11.34 \pm 0.27$, however, we stress the myriad systematic uncertainties associated with each method.

8 BLACK HOLE PARAMETERS

8.1 Black Hole Mass

As discussed in §1 and **D13a**, Goodrich et al. (1996) found IRAS 10214 to have polarised broad emission lines (C III, C IV, Ly- α /N v) with Keck spectro-polarimetry. Under the standard quasar unification model (Antonucci 1993), this is consistent with a dusty toroidal structure obscuring a direct view of the AGN core and its associated broad-line region (BLR). However, a fraction of the BLR emission is scattered off dust and electrons into the observer's line of sight. This polarises the radiation providing a very useful tool in the dissection of AGN. Dust of course reddens the scattered

³ <http://cxc.harvard.edu/cal/ASPECT/celmon/>

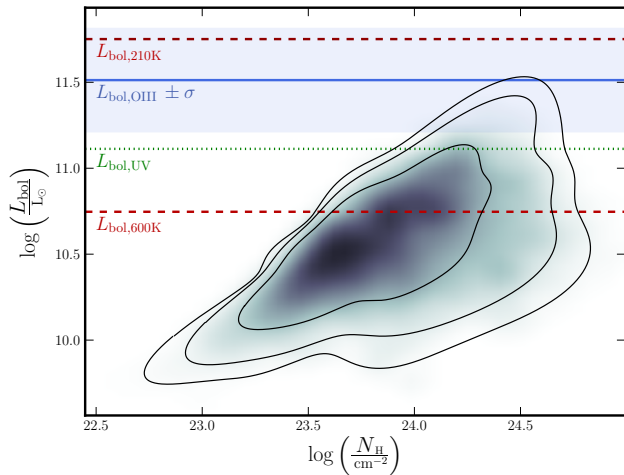


Figure 8. Two dimensional posterior PDF assuming the Wilman & Fabian (1999) X-ray model spectra. The contours correspond to 68, 95 and 99 percent confidence levels. The blue line indicates the bolometric luminosity as derived from the [O III] equivalent width and the blue shaded horizontal band corresponds to the associated 1- σ uncertainty. The two dashed red lines indicate the two dust bolometric luminosity estimates, while the green dotted line is the ultraviolet L_{bol} estimate. Note that the Compton limit is $\sim 10^{24} \text{ cm}^{-2}$. For clarity, we have not included the $L_{\text{bol,UV}}$, $L_{\text{bol,210K}}$ and $L_{\text{bol,600K}}$ uncertainties. They are dominated by the quadrature sum of the covering factor and magnification uncertainties and are of order 0.3-0.5 dex.

radiation, whereas electrons do not alter the spectrum of the incident radiation with any wavelength dependence. Discerning the nature of the scatterers is possible in principle, however not at present in the case of IRAS 10214 due to the low S/N polarised spectrum.

Goodrich et al. (1996) measured a polarised C IV line-width of $\Delta v_{\text{CIV}} \sim 6000 \text{ km s}^{-1}$. Following the Vestergaard & Peterson (2006) calibration, the black hole mass can be estimated from the C IV velocity width via:

$$\log(M_{\text{BH}}(\text{CIV})) = \log\left(\left[\frac{\Delta v_{\text{CIV}}}{1000 \text{ km s}^{-1}}\right]^2 \left[\frac{\lambda L_{\lambda}(1350 \text{ \AA})}{10^{44} \text{ ergs s}^{-1}}\right]^{0.53}\right) + (6.66 \pm 0.01) \quad (3)$$

We determine the value $\nu L_{1350} = 7.3 \times 10^{37} \text{ W}$ based on the quasar bolometric luminosity derived in §7 and an average quasar spectrum (Elvis et al. 1994). This yields a black hole mass of $\log_{10}(M_{\text{BH}}/M_{\odot}) = 8.36 \pm 0.56$. Even with this large uncertainty, this places the black hole mass two orders of magnitude above the ‘knee’ (M^* value) of the $z = 0$ black hole mass function, however it is certainly not amongst the most massive black holes ($> 10^9 M_{\odot}$) observed at this epoch and earlier (e.g. Kurk et al. 2007). Based on this black hole mass and the mean quasar bolometric luminosity derived in §7, we can estimate the Eddington Ratio,

$$\begin{aligned} \eta &= \langle L_{\text{bol,QSO}} \rangle / L_{\text{Edd}} \\ &= 2.2 \times 10^{11} L_{\odot} / 7.4 \times 10^{12} L_{\odot} \\ &= 3_{-2}^{+7} \text{ percent.} \end{aligned} \quad (4)$$

This indicates (even with the large uncertainty) that the accretion rate is likely to be below the typical 10 percent level for actively accreting, radio-loud quasars, consistent with the low intrinsic radio core flux ($S_{1.7\text{GHz}} \sim 3 \mu\text{Jy}$).

While there is some contention regarding the validity of the C IV FWHM as a black hole mass estimator (e.g. Baskin & Laor

2005; Shen et al. 2008; Croom 2011), the polarised C IV line is perhaps the most robust black hole mass estimator we have at our disposal for this obscured quasar. We emphasise the large uncertainty of 0.56 dex as well as the caution raised by Baskin & Laor (2005) regarding the use of the C IV FWHM in black hole mass estimates. Included in this uncertainty is the inclination dependency, since the broad-line region has been shown to be more disc-like rather than spherical (see discussion in Jarvis & McLure 2002, 2006, and references therein). This is the first estimate of the black hole mass in IRAS 10214.

As a consistency check, we estimate the black hole mass, using a second, significantly less secure method based on the rest-frame 5 GHz luminosity and Eddington rate (L/L_{Edd} , Lacy et al. 2001), based on their derived correlation between black hole mass and radio luminosity in the analysis of 60 quasars selected from the FIRST⁴ Bright Quasar Survey (FBQS; Gregg et al. 1996; White et al. 2000). Their correlation is re-arranged as follows:

$$\log_{10}(M_{\text{BH}}) = \frac{\log_{10}(L_{5\text{GHz}}) - 1.0 \log_{10}(L/L_{\text{Edd}}) - 7.9}{1.9}, \quad (5)$$

where M_{BH} is in units of M_{\odot} and $L_{5\text{GHz}}$ is in units of $\text{W Hz}^{-1} \text{ sr}^{-1}$. The scatter in this relation is very large (1.1 dex), since a number of important physical effects are neglected such as black hole spin and Doppler-brightening (Jarvis & McLure 2002). Nonetheless, Equ. 5 does provide an indicative black hole mass, which we calculate assuming the EVN 1.66 GHz (rest-frame 5.5 GHz) flux density of $S_{\text{int}} = 220 \pm 37 \mu\text{Jy}$, its derived magnification of $\mu_{\text{EVN}} = 68$, and accretion rates of $L/L_{\text{Edd}} = 1, 10$ and 100 percent. This results in black hole estimates of $\log_{10}(M_{\text{BH},5\text{GHz}}/M_{\odot}) = 8.79, 8.27, 7.74 \pm 1.1$ for accretion efficiencies of $L/L_{\text{Edd}} = 1, 10$ and 100 percent respectively. The reasonable agreement is encouraging, however we use the C IV FWHM estimate for the remainder of the paper since this method is significantly more robust.

8.2 Black Hole-Spheroid Mass Ratio

Based on the black hole mass estimate in §8.1, we now constrain the intrinsic stellar mass in IRAS 10214 in order to estimate the black hole to stellar mass ratio. We do not attempt a bulge-to-‘disk’ decomposition, since this requires detailed two-dimensional Sersic fitting of the source-plane inversion of a (preferably) pixel-based lensing inversion algorithm which is beyond the scope of this paper. We therefore make the assumption that the bulge mass dominates over the host stellar mass. The tentative 4000 Å break in Lacy, Rawlings, & Serjeant (1998) suggests that an older stellar population, more likely to be concentrated in a bulge, may dominate the rest-frame optical spectrum. The source-plane scale radius of the *HST* F160W component in Deane et al. (in preparation) is $r_s \sim 500 \text{ pc}$ which is significantly smaller than the CO (1→0) source-plane scale radius ($r_{\text{CO}} = 5.7 \text{ kpc}$) derived in D13b. This is consistent with the expectation that a bulge component will have a radius significantly smaller than the extended gas reservoir. Finally, we assume that the stellar mass dominates the *total* mass inside this loosely defined spheroid which is consistent with strong gravitational lensing results coupled with central lens stellar velocity dispersion measurements (Koopmans et al. 2009; Treu & Koopmans 2004). The latter provide constraints on the slope of the total potential which when combined with the light distribution allow

⁴ Faint Images of the Radio SKy at Twenty cm, <http://sundog.stsci.edu>

measurements of the stellar to total mass ratio at the bulge effective radius.

We select the *HST* F160W map to estimate the total magnification since it has a significantly higher S/N than any of the other filters that are dominated by stellar emission. We derive a magnification of $\mu_{\text{stellar}} = 14.1 \pm_{1.2}^{1.6}$ (Deane et al., in preparation), however, we re-emphasise the associated systematic uncertainty described in **D13a** which is in the range of 20-40 percent. The *HST* F160W lensing inversion is part of a detailed lensing analysis of several *HST* filters which is beyond the scope of this paper.

Spectrally-derived stellar mass estimates are challenging in the case of IRAS 10214 since the emission is AGN-dominated in the near-UV and the near-IR with an ill-defined transition into the stellar dominance at optical wavelengths, suggested by the tentative Balmer break. Ideally, we would make a mass estimate in the near-infrared, however, in addition to the AGN emission the lens galaxy makes a substantial, yet unconstrained contribution at this wavelength (Verma et al., in preparation). A compromise is to make a coarse estimate from a single filter that we believe is dominated by stellar continuum emission.

We adopt the *HST* F212N magnitude of $m_{\text{F212N}} = 19.63 \pm 0.34$ determined by Simpson et al. (in preparation) since this wavelength is a less biased tracer of stellar mass and it is the only *HST* filter free of line contamination (Simpson et al., in preparation). The main difference between this and the *HST* F160W map is likely to be dust extinction (between rest frame 490 nm and 650 nm) and therefore does not result in a substantially different solid angle (and hence the resulting magnification) between these two filters. We compare this apparent magnitude with the range of K-corrected *HST* F212N apparent magnitudes derived from a wide range of star formation histories (SFH) using the models of Bruzual & Charlot (2003). We vary the formation redshift between $z_f = 6 - 10$; metallicity between $Z = 0.008 - 0.05$; SFH models include SSP, singular burst and exponential, where the latter have τ values between 0.1 - 5 Gyr. Assuming the *HST* F160W magnification $\mu_{\text{F160W}} = 14.1 \pm_{1.2}^{1.6}$, this results in a range of predicted stellar masses of $\log(M^*(z = 2.3)/M_{\odot}) = 9.6 - 10.6$, and a mean of $\langle \log(M^*(z = 2.3)/M_{\odot}) \rangle = 10.1 \pm 0.5$, where the uncertainties are conservatively assumed to be half the full range.

Our dynamical and gas mass estimates in **D13b**, imply a stellar mass of $M_{\text{stellar,dyn}} = 6.8 \pm 1.7 \times 10^9 M_{\odot}$ which is calculated by assuming the mean gas fraction for a large sample of infrared luminous galaxies (Bothwell et al. 2013) and a dark matter fraction within the CO (1 \rightarrow 0) effective radius (Daddi et al. 2010). The **D13b** stellar mass is in good agreement with our *HST* F212N estimate. The stated assumptions, along with this rough stellar mass of $\langle \log(M^*(z = 2.23)/M_{\odot}) \rangle = 10.1 \pm 0.5$, enable an estimate of the central super-massive black hole to spheroid mass ratio, $M_{\text{BH}}/M_{\text{spheroid}} = 0.02$, admittedly with large uncertainty (~ 0.8 dex). However, this is ~ 1.2 dex larger than the typical ratio found at $z \approx 0$, however both are consistent with the suggested evolution of this relation for AGN host galaxies. For example, assuming $\alpha \sim 2 \pm 1$ (where $\alpha \propto M_{\text{BH}}/M_{\text{spheroid}}$), we expect an increase in the $M_{\text{BH}}/M_{\text{spheroid}}$ relation by a factor of $11 \pm_{8}^{25}$ at a redshift of $z = 2.3$, in agreement with our derived values.

The black hole to spheroid mass ratio is typically $M_{\text{BH}}/M_{\text{spheroid}} \sim 0.1-0.2$ percent at $z \sim 0$ (e.g. Merritt & Ferrarese 2001; Marconi & Hunt 2003; Häring & Rix 2004), but as stated above, are found to increase for high-redshift quasars, albeit with large uncertainty and selection effects, by a number of authors (e.g. Peng et al. 2006; McLure et al. 2006; Treu et al. 2007; Bennert et al. 2011). Peng et al. (2006) investigated a

sample of 31 gravitationally-lensed and 20 non-lensed AGN and found that the $M_{\text{BH}}/M_{\text{bulge}}$ mass increased by a factor of $\gtrsim 4 \pm^2_1$ for $z > 1.7$. McLure et al. (2006) performed a similar study with the 3CRR sample (Laing et al. 1983), which consisted of 170 radio-loud, low-frequency selected AGN. They found an evolution of $M_{\text{BH}}/M_{\text{spheroid}} \propto (1+z)^{\alpha}$ where $\alpha = 2.07 \pm 0.76$. Treu et al. (2007) and Bennert et al. (2011) find a consistent values of $\alpha = 1.5 \pm 1.0; 1.96 \pm 0.55$ for samples with mean redshifts of $z \sim 0.36$ and $z \sim 2$ respectively. The former sample was made up of 20 Seyferts, while the latter comprised of 11 X-ray selected, broad-line AGN in a GOODS-N/S sample. There are clearly a number of independent studies that suggest quasar black hole growth precedes the full development of the stellar component to some degree, however, selection biases could yield similar results, as argued in Lauer et al. (2007).

Although the uncertainties are large, the overall picture strongly supports that the majority of the black hole growth precedes the stellar mass assembly for this obscured quasar (assuming that IRAS 10214 will evolve to be consistent with the local $M_{\text{BH}}/M_{\text{spheroid}}$ relation). This is contrary to the ‘under-massive’ black hole masses measured in $z \sim 2$ SMGs by Alexander et al. (2008) and Biggs, Younger, & Ivison (2010). Alexander et al. (2008) made M_{BH} estimates in 6 broad line SMGs using H β and H α line-widths using the Greene & Ho (2005) virial estimator, and found that (a) they have black hole masses $\gtrsim 3$ times smaller than ‘normal’ galaxies in the local Universe of comparable mass; and (b) they have $\gtrsim 10$ times smaller black holes masses than that predicted for $z \sim 2$ populations. From their Fig. 4, they derive a $M_{\text{BH}}/M_{\text{spheroid}}$ ratio $\approx 2.5 - 4 \times 10^{-4}$ for the CO-dynamics and stellar mass determined bulge mass. Biggs, Younger, & Ivison (2010) performed a VLBI survey of 6 SMGs with a mean redshift of $z \sim 2$. They calculate black hole masses (and upper limits) based on the Lacy et al. (2001) $L_{5\text{GHz}}$ method and their 1.6 GHz VLBI observations of all 6 SMGs. Although the uncertainty is very large (1.1 dex), all 6 of their objects have black hole masses (or upper limits) that are $\sim 0.2 - 1.3$ dex below the expected value based on the Häring & Rix (2004) finding that $M_{\text{BH}}/M_{\text{spheroid}} = 0.0014 \pm 0.0004$ in the local Universe. The mean of their quoted stellar masses and black holes masses (as well as upper limits) implies a $\log(M_{\text{BH}}/M_{\text{spheroid}}) \approx 0.0002$ with the quoted uncertainty of 1.1 dex.

Despite the large uncertainties, there appears to be 1-2 orders of magnitude difference between the black hole to spheroid mass ratio in SMGs and the obscured quasar IRAS 10214. This tentatively implies very different evolutionary paths for these two object classes, despite their apparent similarities in many parts of the global SED. However, this may be a result of the selection bias outlined in Lauer et al. (2007), particularly since we demonstrate in this work that the AGN is preferentially magnified by an order of magnitude when compared to the spatially-resolved *JVLA* CO (1 \rightarrow 0) map in **D13b**.

Nonetheless, the high $M_{\text{BH}}/M_{\text{spheroid}}$ ratio, relatively regular CO (1 \rightarrow 0) velocity map (**D13b**), single *EVN* detection, highly magnified yet uniform *HST* F160W morphology, are all consistent with IRAS 10214 being an example of a fairly typical AGN-host galaxy at $z \sim 2$, as found in Kocevski et al. (2012). These authors present deep *HST* F160W (*H*-band) and *HST* F125W (*J*-band) observations of 72 intermediate X-ray luminosity ($L_X \sim 10^{42-44}$ erg s $^{-1}$) AGN selected from the 4 Ms *Chandra* observation of the *Chandra* Deep Field South, as part of the CANDELS survey (Grogin et al. 2011). They find that AGN host galaxies at $z \sim 2$ appear no more likely to be part of a major merger than a control sample of galaxies in the same mass range. One caveat, how-

ever, is that most major merger traits may be erased by the time the resultant AGN activity begins. The Kocevski et al. (2012) result is consistent with Schawinski et al. (2012) who show that a sample of $z \sim 2$ highly obscured quasar host galaxies are not major mergers, but have reasonably smooth morphologies with Sérsic indices consistent with disks. Furthermore, Cisternas et al. (2011) and Georgakakis et al. (2009) find consistent results at $z \sim 1$. These results form part of a growing consensus that major mergers do not play the dominant role in triggering intermediate luminosity AGN activity as outlined in the classical Sanders et al. (1988) scenario, where the merger-induced loss of angular momentum leads to black hole accretion. Moreover, these studies all find that AGN-hosts at $z \sim 1 - 3$ are predominantly disk-like in morphology, which is what the CO (1 \rightarrow 0) kinematics tentatively suggest for IRAS 10214 (**D13b**).

This paper (together with the series it forms part of) therefore suggests that IRAS 10214 hosts a super-massive black hole that has primarily grown in mass due to secular evolution, minor interactions and/or internal instabilities, rather than the classical major merger-induced scenario. We propose that IRAS 10214 is therefore a relatively typical intermediate luminosity AGN at $z \sim 2$, however its active nucleus is preferentially-lensed by an order of magnitude with respect to the star forming disk.

9 CONCLUSIONS

We have performed a deep ($\sigma = 23 \mu\text{Jy beam}^{-1}$), 1.7 GHz *EVN* observation on IRAS 10214, a lensed $z = 2.3$ obscured quasar with prodigious star formation. The VLBI observation provides a brightness temperature filter which is unobscured by dust and therefore allows us to image the obscured active nucleus with an effective angular resolution of $\lesssim 50$ pc at $z = 2.3$, after correcting for gravitational lensing. These *EVN* observations permit a number of conclusions to be drawn:

(i) The AGN core as traced by the *EVN* 1.7 GHz detection has a flux density peak of $S_{\text{peak}} = 209 \pm 23 \mu\text{Jy beam}^{-1}$ which makes up ~ 20 percent of the total 1.7 GHz flux density of a *MERLIN* map presented in **D13a**. The *EVN* detection appears unresolved, with an integrated flux density of $S_{\text{peak}} = 220 \pm 37 \mu\text{Jy}$. The remainder of the *MERLIN* 1.7 GHz flux is likely to be split between star formation and large-scale ($\gtrsim 200$ pc) jets.

(ii) The fact that the AGN core is a single detection and is northward of the *HST* F814W arc, strongly advocates that the *HST* F814W arc is not a triple-image system that is merged by the *HST* PSF. This supports the lens model derived by **D13a** which suggests that the *HST* F814W map is comprised of a single arc and the observed double peak corresponds to intrinsic structure at rest-frame ultraviolet wavelengths.

(iii) The AGN core is located at a position qualitatively consistent with the spatially-resolved polarisation properties of the ultraviolet map reported in Nguyen et al. (1999). Moreover, it is consistent with their prediction of the active nucleus position based on these polarisation properties as well as the narrowband *HST* observations which suggest that the BLR centre-of-curvature is northward of the NLR centre-of-curvature (Simpson et al., in preparation).

(iv) If the AGN core position and size are well approximated by the radio core detected in this *EVN* observation, then the AGN is preferentially magnified by over an order of magnitude when compared to a spatially resolved *JVLA* CO (1 \rightarrow 0) map (**D13b**), where the latter can be used as a star formation proxy. This confirms

the effective ‘chromaticity’ of this strong-lens system (discussed in **D13a**, **D13b**), which is caused by different emission regions undergoing differing magnification boosts due to their relative size and position with respect to the caustic. This effect may be particularly relevant in the case of far-infrared (FIR) bright, strongly-lensed galaxies discovered by the *Herschel Space Observatory* (Negrello et al. 2010).

(v) The configuration of the *EVN* core and *HST* ultraviolet arc support our previous claim that this is an asymmetric (or one-sided) source where we observe the line-of-sight NLR, whilst the ‘counter-NLR’ is obscured by a significant host dust reservoir, consistent with examples in the nearby Universe (e.g. Liu & Pooley 1991; Simpson et al. 1997).

(vi) We derive a black hole mass of $\log_{10}(M_{\text{BH}}/M_{\odot}) = 8.36 \pm 0.56$ and a bolometric luminosity $\log_{10}(\langle L_{\text{bol, QSO}} \rangle / L_{\odot}) = 11.34 \pm 0.27$ dex, which suggests a low accretion rate $\eta \sim 3 \pm 2$ percent, albeit with significant uncertainty.

(vii) Our crudely derived black hole to spheroid mass ratios are consistent with the suggested evolution of this parameter in AGN host galaxies (Peng et al. 2006; McLure et al. 2006; Treu et al. 2007; Bennert et al. 2011). The $M_{\text{BH}}/M_{\text{spheroid}}$ ratio in IRAS 10214 is 1-2 orders of magnitude larger than that of $z \sim 2$ SMGs based on optical and radio analyses (Alexander et al. 2008; Biggs, Younger, & Ivison 2010), providing a tentative suggestion that these two object classes may follow different evolutionary paths (i.e. secular rather than merger-induced black hole growth). However, this picture is sensitive to the large black hole mass uncertainties and selection effects (e.g. Lauer et al. 2007).

These results point toward a intermediate luminosity AGN, however our X-ray modelling find it to be a highly obscured nucleus. The mean hydrogen column density $\bar{N}_{\text{H}} \sim 10^{23.5} \text{ cm}^{-2}$ explains the excessive [O III] $\lambda 5007$ luminosity in comparison with the derived X-ray luminosity (Alexander et al. 2008). This X-ray modelling predicts a strong Fe K line to be observed if the required sensitivity is achieved. The unobscured, intrinsic quasar bolometric luminosity ($2.2 \times 10^{11} L_{\odot}$) is well supported with independent bolometric luminosity estimates and suggests inefficient, sub-Eddington accretion onto the central black hole which is consistent with the low intrinsic radio core flux ($S_{1.7\text{GHz}} \sim 3 \mu\text{Jy}$). Comparison with a large sample of AGN host galaxies at $z \sim 1.5 - 2.5$ (Kocevski et al. 2012) suggests that IRAS 10214 is plausibly a fairly typical AGN host based on the lack of major merger traits and the relatively regular CO (1 \rightarrow 0) velocity map, consistent with a disk-like morphology. Therefore, the key difference in the case of IRAS 10214 may be that it has a preferentially magnified active nucleus. This case study is not only a clear demonstration of the significant SED distortion due to preferential lensing, but also a preview of what can be achieved with the enhanced sensitivity and new wide-field capabilities of the *VLBA* as well as the *EVN* which will detect large samples of low-luminosity AGN ($L_{5\text{GHz}} \lesssim 10^{22} \text{ W Hz}^{-1} \text{ sr}^{-1}$) over well-studied multi-wavelength fields (e.g. Middelberg et al. 2011). These surveys will play an important role in characterising AGN activity over cosmic time, particularly for the obscured AGN population.

ACKNOWLEDGMENTS

This paper, as well as the series it forms a part of, is dedicated to the memory of Steve Rawlings. We are grateful to the *EVN* chair for awarding discretionary telescope time to perform a calibrator

search in the vicinity of the target source - this was key to the success of the observation of IRAS 10214. We thank Zsolt Paragi who generously provided technical expertise in the planning and execution of the EVN observations. The European VLBI Network is a joint facility of European, Chinese, South African and other radio astronomy institutes funded by their national research councils. The National Radio Astronomy Observatory is a facility of the National Science Foundation operated under cooperative agreement by Associated Universities, Inc. This work made use of the Swinburne University of Technology software correlator, developed as part of the Australian Major National Research Facilities Programme and operated under licence. This effort/activity was supported by the European Community Framework Programme 6 and 7, Square Kilometre Array Design Studies (SKADS), contract no. 011938; and PrepSKA, grant agreement no.: 212243. RPD gratefully acknowledges funding that enabled visits to JIVE which were supported by the European Community Framework Programme 7, Advanced Radio Astronomy in Europe, grant agreement no.: 227290. PJM acknowledges support from the Royal Society in the form of a University Research Fellowship.

REFERENCES

- Alexander D. M., Chartas G., Bauer F. E., Brandt W. N., Simpson C., Vignali C., 2005, *MNRAS*, 357, L16
- Alexander, D. M., Brandt, W. N., Smail, I., et al. 2008, *AJ*, 135, 1968
- Antonucci R., 1993, *ARA&A*, 31, 473
- Ao Y., Weiß A., Downes D., Walter F., Henkel C., Menten K. M., 2008, *A&A*, 491, 747
- Baskin A., Laor A., 2005, *MNRAS*, 356, 1029
- Bennert V. N., Auger M. W., Treu T., Woo J.-H., Malkan M. A., 2011, *ApJ*, 742, 107
- Biggs A. D., Younger J. D., Ivison R. J., 2010, *MNRAS*, 408, 342
- Blandford R. D., Kochanek C. S., Kovner I., Narayan R., 1989, *Sci*, 245, 824
- Bothwell, M. S., Smail, I., Chapman, S. C., et al. 2013, *MNRAS*, 429, 3047
- Bruzual, G., & Charlot, S. 2003, *MNRAS*, 344, 1000
- Chen, B., Dai, X., Kochanek, C. S., et al. 2012, *arXiv:1202.5304*
- Cisternas, M., Jahnke, K., Inskip, K. J., et al. 2011, *ApJ*, 726, 57
- Condon J. J., 1997, *PASP*, 109, 166
- Croom S. M., 2011, *ApJ*, 736, 161
- Daddi E., et al., 2010, *ApJ*, 713, 686
- Deane, R. P., Rawlings, S., Marshall, P. J., et al. 2013, *MNRAS*, 430, 2
- Deane R. P., et al., 2013, *MNRAS*, 1747
- Downes D., Solomon P. M., 1998, *ApJ*, 507, 615
- Dunlop J. S., Peacock J. A., 1990, *MNRAS*, 247, 19
- Dyer, C. C., & Shaver, E. G. 1992, *ApJL*, 390, L5
- Eales S., et al., 2010, *PASP*, 122, 499
- Eisenhardt P. R., Armus L., Hogg D. W., Soifer B. T., Neugebauer G., Werner M. W., 1996, *ApJ*, 461, 72
- Efstathiou A., 2006, *MNRAS*, 371, L70
- Elmegreen, B. G. 1999, *ApJ*, 517, 103
- Elston, R., McCarthy, P. J., Eisenhardt, P., et al. 1994, *AJ*, 107, 910
- Elmegreen B. G., 1999, *ApJ*, 517, 103
- Elvis M., et al., 1994, *ApJS*, 95, 1
- Evans A. S., Scoville N. Z., Dinshaw N., Armus L., Soifer B. T., Neugebauer G., Rieke M., 1999, *ApJ*, 518, 145
- Fabian, A. C., Cutri, R. M., Smith, H. E., Crawford, C. S., & Brandt, W. N. 1996, *MNRAS*, 283, L95
- Ferrarese L., Merritt D., 2000, *ApJ*, 539, L9
- Fiore F., et al., 2008, *ApJ*, 672, 94
- Gebhardt K., et al., 2000, *ApJ*, 539, L13
- Georgakakis, A., Coil, A. L., Laird, E. S., et al. 2009, *MNRAS*, 397, 623
- Gilli, R., Comastri, A., & Hasinger, G. 2007, *A&A*, 463, 79
- Goodrich R. W., Miller J. S., Martel A., Cohen M. H., Tran H. D., Ogle P. M., Vermeulen R. C., 1996, *ApJ*, 456, L9
- Greene, J. E., & Ho, L. C. 2005, *ApJ*, 630, 122
- Gregg M. D., Becker R. H., White R. L., Helfand D. J., McMahon R. G., Hook I. M., 1996, *AJ*, 112, 407
- Grogin, N. A., Kocevski, D. D., Faber, S. M., et al. 2011, *ApJS*, 197, 35
- Häring N., Rix H.-W., 2004, *ApJ*, 604, L89
- Helmboldt J. F., et al., 2007, *ApJ*, 658, 203
- Iwasawa K., Vignali C., Evans A. S., Sanders D. B., Trentham N., 2009, *arXiv*, *arXiv:0905.3512*
- Jarvis, M. J., & McLure, R. J. 2002, *MNRAS*, 336, L38
- Jarvis M. J., McLure R. J., 2006, *MNRAS*, 369, 182
- Keeton C. R., Gaudi B. S., Petters A. O., 2003, *ApJ*, 598, 138
- Kettenis M., van Langevelde H. J., Reynolds C., Cotton B., 2006, *ASPC*, 351, 497
- Klöckner H.-R., Martínez-Sansigre A., Rawlings S., Garrett M. A., 2009, *MNRAS*, 398, 176
- Koopmans, L. V. E., Biggs, A., Blandford, R. D., et al. 2003, *ApJ*, 595, 712
- Koopmans, L. V. E., Bolton, A., Treu, T., et al. 2009, *ApJL*, 703, L51
- Kocevski, D. D., Faber, S. M., Mozena, M., et al. 2012, *ApJ*, 744, 148
- Kurk, J. D., Walter, F., Fan, X., et al. 2007, *ApJ*, 669, 32
- Lacy M., Rawlings S., Serjeant S., 1998, *MNRAS*, 299, 1220
- Lacy M., Laurent-Muehleisen S. A., Ridgway S. E., Becker R. H., White R. L., 2001, *ApJ*, 551, L17
- Lauer, T. R., Tremaine, S., Richstone, D., & Faber, S. M. 2007, *ApJ*, 670, 249
- Lawrence A., et al., 1993, *MNRAS*, 260, 28
- Laing, R. A., Riley, J. M., & Longair, M. S. 1983, *MNRAS*, 204, 151
- Liu R., Pooley G., 1991, *MNRAS*, 253, 669
- Madau P., Ferguson H. C., Dickinson M. E., Giavalisco M., Steidel C. C., Fruchter A., 1996, *MNRAS*, 283, 1388
- Magorrian J., et al., 1998, *AJ*, 115, 2285
- Marconi A., Hunt L. K., 2003, *ApJ*, 589, L21
- Martínez-Sansigre A., Rawlings S., Lacy M., Fadda D., Marleau F. R., Simpson C., Willott C. J., Jarvis M. J., 2005, *Nature*, 436, 666
- Madau P., Ghisellini G., Fabian A. C., 1994, *MNRAS*, 270, L17
- McKean J. P., et al., 2007, *MNRAS*, 378, 109
- McLure R. J., Jarvis M. J., Targett T. A., Dunlop J. S., Best P. N., 2006, *MNRAS*, 368, 1395
- Merritt, D., & Ferrarese, L. 2001, *MNRAS*, 320, L30
- Middelberg, E., Deller, A., Morgan, J., et al. 2011, *A&A*, 526, A74
- Miller P., Rawlings S., Saunders R., Eales S., 1992, *MNRAS*, 254, 93
- Mor R., Netzer H., Elitzur M., 2009, *ApJ*, 705, 298
- More A., McKean J. P., More S., Porcas R. W., Koopmans L. V. E., Garrett M. A., 2009, *MNRAS*, 394, 174

- Muxlow T. W. B., Pedlar A., Wilkinson P. N., Axon D. J., Sanders E. M., de Bruyn A. G., 1994, MNRAS, 266, 455
- Nguyen H. T., Eisenhardt P. R., Werner M. W., Goodrich R., Hogg D. W., Armus L., Soifer B. T., Neugebauer G., 1999, AJ, 117, 671
- Negrello M., et al., 2010, Sci, 330, 800
- Netzer, H., Mainieri, V., Rosati, P., & Trakhtenbrot, B. 2006, A&A, 453, 525
- Pei Y. C., 1992, ApJ, 395, 130
- Peng, C. Y., Impey, C. D., Rix, H.-W., et al. 2006, ApJ, 649, 616
- Polletta M. d. C., et al., 2006, ApJ, 642, 673
- Pooley D., Blackburne J. A., Rappaport S., Schechter P. L., 2007, ApJ, 661, 19
- Rowan-Robinson, M., Broadhurst, T., Oliver, S. J., et al. 1991, Nat, 351, 719
- Rowan-Robinson M., et al., 1993, MNRAS, 261, 513
- Sanders, D. B., Soifer, B. T., Elias, J. H., et al. 1988, ApJ, 325, 74
- Schawinski, K., Simmons, B. D., Urry, C. M., Treister, E., & Glikman, E. 2012, MNRAS, L488
- Schweitzer M., et al., 2007, ASPC, 373, 501
- Scoville N. Z., Yun M. S., Bryant P. M., 1997, ApJ, 484, 702
- Serjeant S., Rawlings S., Lacy M., McMahon R. G., Lawrence A., Rowan-Robinson M., Mountain M., 1998, MNRAS, 298, 321
- Shen, Y., Greene, J. E., Strauss, M. A., Richards, G. T., & Schneider, D. P. 2008, ApJ, 680, 169
- Shi Y., et al., 2006, ApJ, 653, 127
- Simpson C., Wilson A. S., Bower G., Heckman T. M., Krolik J. H., Miley G. K., 1997, ApJ, 474, 121
- Soifer, B. T., Cohen, J. G., Armus, L., et al. 1995, ApJL, 443, L65
- Spergel D. N., et al., 2007, ApJS, 170, 377
- Sturm E., Hasinger G., Lehmann I., Mainieri V., Genzel R., Lehnert M. D., Lutz D., Tacconi L. J., 2006, ApJ, 642, 81
- Teplitz H. I., et al., 2006, ApJ, 638, L1
- Thompson T. A., Quataert E., Murray N., 2005, ApJ, 630, 167
- Treu, T., & Koopmans, L. V. E. 2004, ApJ, 611, 739
- Treu, T., Woo, J.-H., Malkan, M. A., & Blandford, R. D. 2007, ApJ, 667, 117
- Tristram K. R. W., et al., 2009, A&A, 502, 67
- Tristram K. R. W., Schartmann M., 2011, arXiv, arXiv:1105.4875
- Vestergaard M., Peterson B. M., 2006, ApJ, 641, 689
- White R. L., et al., 2000, ApJS, 126, 133
- Wilman, R. J., Fabian, A. C., Cutri, R. M., Crawford, C. S., & Brandt, W. N. 1998, MNRAS, 300, L7
- Wilman R. J., Fabian A. C., 1999, MNRAS, 309, 862